



**Politecnico
di Torino**

PRELIMINARY ANALYSIS OF A STANDARD CO₂ EMISSIONS METRIC SYSTEM FOR A LARGE BUSINESS JET

Laurea Magistrale in Ingegneria Aerospaziale
A.A 2023-2024

Relatrice: Prof.ssa Viola Nicole
Co-relatore: Dr. Ferretto Davide
Co-relatore: Dr. Gori Oscar
Co-relatore: Ing. Graziani Samuele

Candidata: Capocasale Rossella

A mio fratello,
ai miei genitori.

SUMMARY

SUMMARY	4
LIST OF TABLES	7
LIST OF FIGURES	10
ABSTRACT	13
Capitolo 1 INTRODUCTION	14
1.1 Business Jets: a shrinking world	14
1.2 Use of Business Jet	15
1.3 Birth and development of private aviation.....	15
1.4 Future trends	16
1.5 Environmental Impact of Business Jets	17
1.6 Categories	19
1.7 Development and purpose of the thesis	21
Capitolo 2 CASE STUDY DESCRIPTION	23
2.1 Description of Falcon 10 X.....	23
2.1.1 Dimensions	24
2.1.2 Performance data	24
2.1.3 Engines and avionics	25
2.1.4 Mission type.....	26
2.2 Conceptual Design of Falcon 10 X.....	28
2.2.1 Aircraft and mission requirements.....	28
2.2.2 Wing and fuselage geometry	29
2.2.3 Tail geometry.....	30
2.2.4 CAD model.....	31
Capitolo 3 CO ₂ METRIC VALUE ACQUISITION– LOW-FIDELITY ANALYSIS	33
3.1 Aerodynamics simulation	33
3.1.1 Aerodynamic forces.....	33
3.1.2 Aerodynamic coefficients.....	34

3.2 Simulation of the Propulsion System.....	37
3.2.1 On-design analysis.....	37
3.2.2 Off-design analysis.....	40
3.3 Mission simulation.....	42
3.3.1 ASTOS - Advanced Simulation Tool for Space Operations.....	42
3.3.2 Mission type.....	42
3.3.3 Simulation setting.....	43
3.3.4 Phase definition: Climb, Cruise, Approach.....	44
3.4 Application of the standard.....	46
3.4.1 CO ₂ metric value definition.....	46
3.4.2 SAR calculation.....	47
3.4.3 RGF calculation.....	49
3.4.4 Valutation of CO ₂ metric value.....	52
Capitolo 4 CO ₂ METRIC VALUE ACQUISITION – HIGH-FIDELITY ANALYSIS.....	53
4.1 Aerodynamics simulation.....	53
4.1.1 Mesh.....	53
4.1.2 Solver description – Ansys Fluent.....	58
4.1.3 Eulero equations.....	59
4.1.4 Riemann problem.....	61
4.1.5 Approximate Riemann solvers – Roe’s method (1981).....	62
4.1.6 Simulation setting.....	64
4.1.7 Test matrix.....	66
4.2 Mission simulation.....	68
4.3 Application of the standard.....	70
Capitolo 5 DISCUSSION OF RESULTS.....	72
5.1 Discussion of the aerodynamics simulation’s results.....	72
5.1.1 Comparison of Raymer model and CFD results – Lift coefficient.....	72
5.1.2 Comparison of Raymer model and CFD results – Drag coefficient.....	73
5.2 Discussion of Propulsion System simulation’s results.....	75
5.2.1 Mattingly Equations Considerations.....	75
5.2.2 Nominal Thrust Considerations.....	76
5.3 Discussion of mission simulation’s results.....	77
5.3.1 Low fidelity analysis.....	77
5.3.2 High fidelity analysis.....	77

5.3.3 Comparison of Mission Profiles	78
5.4 Discussion of CO ₂ metric values obtained.....	79
5.4.1 The low fidelity CO ₂ metric value: based on present masspoints vs based on real cruise points.....	79
5.4.2 The high fidelity CO ₂ metric value: based on present masspoints vs based on real cruise points.....	82
Capitolo 6 CONCLUSIONS	86
REFERENCES	88

LIST OF TABLES

Table 1.1: Business Jet categories.....	20
Table 2.1: Falcon 10 X dimensions	24
Table 2.2: Falcon 10 X performance data.....	25
Table 2.3: Falcon 10 X engines and avionics data.....	25
Table 2.4: Possible connections for the Falcon 10 X: in green are the possible connections, in red those that cannot be made without making stopovers and refuelling	28
Table 2.5: Requirements	29
Table 2.6: Inputs for wing design	29
Table 2.7: Outputs for wing design.....	29
Table 2.8: Fuselage geometry	30
Table 2.9: Vertical tail geometry	30
Table 2.10: Horizontal tail geometry	30
Table 3.1: FF calculation	36
Table 3.2: Qc values	37
Table 3.3: Requirements of the propulsion system.....	39
Table 3.4: Performances on design point.....	39
Table 3.5: Mach, Throttle and Altitude settings	40
Table 3.6: Flight phases settings.....	42
Table 3.7: Results of off-design analysis	42
Table 3.8: Flight phases	43
Table 3.9: CO ₂ maximum permitted metric value	47
Table 3.10: Gross masses.....	47
Table 3.11: Air values for γ and R	48
Table 3.12: SAR calculation: temperature, sound speed, Mach number, TAS, fuel mass flow, SAR.....	48
Table 3.13: 1SARAVG calculation.....	48
Table 3.14: Calculation of the floor hight.....	51
Table 3.15: RGF results	51

Table 3.16: CO ₂ metric value.....	52
Table 4.1: Computational domain dimensions	54
Table 4.2: Elements' shape and number	55
Table 4.3: Mach numbers and angles of attack.....	65
Table 4.4: Atmosphere conditions at 12000 m	65
Table 4.5: Reference values	66
Table 4.6: Test matrix, I and II order accuracy.....	67
Table 4.7: SAR calculation: temperature, sound speed, Mach number, TAS, fuel mass flow, SAR.....	70
Table 4.8: 1SARAVG calculation.....	71
Table 4.9: CO ₂ metric value.....	71
Table 5.1: Estimation of actual thrust values	75
Table 5.2: Estimation of actual SFC values.....	76
Table 5.3: Nominal Thrust considerations.....	76
Table 5.4: Comparison of distance flown and declared range – Low fidelity analysis	77
Table 5.5: Comparison of distance flown and declared range – High fidelity analysis....	78
Table 5.6: New gross masses vs old ones	80
Table 5.7: 1SARAVG calculation.....	80
Table 5.8: Comparison of the two CO ₂ metric values	81
Table 5.9: New gross masses vs old ones	83
Table 5.10: 1SARAVG calculation.....	83
Table 5.11: Comparison of the two CO ₂ metric values	84

LIST OF FIGURES

Figure 1.1: Business Jet Sales 2008 to 2023	16
Figure 1.2: Business Jet Market Forecast by Forecast International.....	17
Figure 1.3: Example of a GLF6 flight and estimation of its CO2 emissions	18
Figure 1.4: CO2 emissions of 250 private jets between 2019 and 2022.....	19
Figure 1.5: Business Jet categories	20
Figure 2.1: Falcon 10 X	23
Figure 2.2:Rolls-Royce Pearl 10 X.....	26
Figure 2.3: NASA SC-0610.....	30
Figure 2.4: NACA 0010.....	31
Figure 2.5: CAD and dimensions – 1 frontal view, 2 lateral view, 3 top view.....	32
Figure 3.1: Origin of aerodynamic forces.....	34
Figure 3.2: Lift - Raymer model.....	35
Figure 3.3: Drag - Raymer model.....	37
Figure 3.4: Turbofan scheme	38
Figure 3.5: Specific Thrust vs Specific Thrust Fuel Consumption.....	39
Figure 3.6:Turbofan engine with losses vs πc and α	39
Figure 3.7:Turbofan engine with losses vs πc and α	40
Figure 3.8: Evolution of turbine entry temperature and future trend (Kyprianidi 2011)	41
Figure 3.9: Thrust vs Altitude at different Mach numbers.....	41
Figure 3.10: Altitude, Mach number vs time	45
Figure 3.11: Angle of attack, pitch vs time.....	45
Figure 3.12: Thrust, drag force vs time.....	46
Figure 3.13: Propellant mass flow	46
Figure 3.14: Location of gross masses within the mission profile.....	49
Figure 3.15: SAR – mass/MTOM.....	49
Figure 3.16: RGF	50
Figure 3.17: Examples of Fuselage Outer Mould Line (OML) e Floor Area; at the centre the case of Falcon 10 X.....	50

Figure 3.18: Floor plane.....	51
Figure 3.19: Section on the floor plane.....	51
Figure 3.20: Section on the floor plane – zoom.....	52
Figure 3.21: Comparison with the maximum permitted metric value of CO ₂	52
Figure 4.1: Parts of the computational domain: 1 inlet and outlet, 2 inlet and outlet far field, 3 inlet external layer.....	55
Figure 4.2: Mesh views: 1-2 diagonal, 3 front, 4 retro, 5-6 lateral.....	58
Figure 4.3: Signals for a subsonic case of study.....	62
Figure 4.4: Diagram for computing interface flux.....	64
Figure 4.5: Lift coefficient – I order.....	67
Figure 4.6: Drag coefficient – I order.....	67
Figure 4.7: Moment coefficient – I order.....	67
Figure 4.8: Lift coefficient - II order.....	68
Figure 4.9: Drag coefficient - II order.....	68
Figure 4.10: Moment coefficient - II order.....	68
Figure 4.11: Altitude, Mach number vs time.....	69
Figure 4.12: Angle of attack, Pitch angle vs time.....	69
Figure 4.13: Thrust, Drag force vs time.....	70
Figure 4.14: Propellant mass vs time.....	70
Figure 4.15: Comparison with the maximum permitted metric value of CO ₂	71
Figure 5.1: Lift coefficient - M=0.3, M=0.6.....	73
Figure 5.2: Lift coefficient - M=0.8, M=0.9.....	73
Figure 5.3: Drag coefficient - M=0.3, M=0.6.....	74
Figure 5.4: Drag coefficient - M=0.8, M=0.9.....	75
Figure 5.5: Altitude comparison - Low-fidelity vs. high-fidelity analysis.....	78
Figure 5.6: Mach number comparison - Low-fidelity vs. high-fidelity analysis.....	79
Figure 5.7: Gross masses within the Mach number profile – Low fidelity analysis.....	80
Figure 5.8: New gross masses within the Mach number profile – Low fidelity analysis.....	81
Figure 5.9: Comparison of the two CO ₂ metric values and max permitted CO ₂ value – Low fidelity analysis.....	82
Figure 5.10: Gross masses within the Mach number profile – High fidelity analysis.....	83
Figure 5.11: New gross masses within the Mach number profile – Low fidelity analysis.....	84
Figure 5.12: Comparison of the two CO ₂ metric values and max permitted CO ₂ value – High fidelity analysis.....	85

ABSTRACT

The environmental impact of private jets contribute to global aviation emissions, estimated at 3% of total emissions. Private jets, though carrying few passengers, can emit tens of tonnes of CO₂ per flight, highlighting the inequality in emissions compared to average global citizens, whose annual carbon footprint is around 4.7 tonnes: already from these figures one can see the importance and necessity of having adequate standard for business aviation. The aim of this thesis is to define the CO₂ emission requirements of the Business Jet category, starting from a comparison with the regulations currently in force, specialising in the regulation of emissions from civil aviation aircraft. The regulations in question were issued by ICAO in 2017 and are called *Annex 16 - Volume III, "CO₂ emission requirements"* and provide the entire logical procedure to be used in order to calculate the CO₂ metric value of each aircraft to which the regulations refer, also providing the metric limit value not to be exceeded.

In order to be able to apply the requirements of the regulations, it was necessary to choose a case study and analyse it both from an aerodynamic point of view - first by applying the Raymer model, then by means of CFD techniques - and from a propulsion and mission point of view. The protagonist of the analysis is an ultra-long-range business jet based on the Dassault's Falcol 10 X concept, which is currently in the production phase and of which, therefore, no emission data is yet available. In any case, even if such data were available, there would be no current specific standard, regarding emissions from the business jet category, that could decide the suitability of the new jet; the final step of this thesis work is therefore to apply the standard, to see if it can be still valid for the case study or, alternatively, to propose analytical reports to be applied in place of those presented in the ICAO document.

Capitolo 1

INTRODUCTION

Chapter 1 introduces the figure of the business jet, setting it in a social and economic context. Firstly, the reasons why more and more people are buying private aircraft are investigated and the uses to which they will be put are identified. Then, the current market is observed and an attempt is made to understand which direction it will take in the future, in order to obtain information on the trend that jet buying and production is undertaking. This step is crucial in order to establish the extent to which these aircraft will be used in the future, as more and more attention is being paid to their emissions in relation to the issue of environmental impact. In this regard, an initial study on the emissions of a sample of business jets is presented in order to give a numerical description of the phenomenon. In the last two paragraphs, the various existing categories of Business Jets are presented and the structure of the thesis is discussed in detail.

1.1 Business Jets: a shrinking world

Nowadays, flying is becoming more and more routine and frequent, designating the aircraft as an indicator of the affluence of the age in which it is used. The category of private aviation deserves a separate discussion. It has always been aimed at a small segment of the population, characterised by a high status quo and with needs that do not always fall within the scope of an ordinary holiday. Users of such services include prominent personalities in world politics, who are required to make regular international business trips. They have come to prefer private aviation because of security issues, the rapid increase in passenger numbers in the 20th century, and the terrorist threats that can be hidden in the overcrowded airport environment. However, the needs are not always as serious as in these cases: increasingly, business jets are being used to assert a privileged social status, to travel without interacting with the masses, in absolute comfort and speed.

Whether out of necessity or for leisure, the private aviation market is growing steadily and, for those who can take advantage of it, the world is no longer a difficult place to visit: routes

become shorter, times tighter and more distant destinations become closer. A private jet therefore becomes an instrument that provides unlimited access to global mobility.

1.2 Use of Business Jet

Among the most common uses of business jets is certainly leisure. Turning our attention now to business-related uses, we see that business aviation companies cover a variety of professions, but they all have in common the need for fast, flexible, safe and economical access to destinations around the world. No less important is the possibility for businessmen and women and their teams to plan and work on board the aircraft itself.

Business aviation is also exploited for purposes of scientific research and study of the territory, while another slice is occupied by uses related to emergency situations, such as humanitarian missions.

Regarding the last point, there is no doubt the contribution of private aviation in facilitating humanitarian efforts, ensuring the delivery of emergency supplies and sending medical personnel to remote locations. The diplomatic sphere has also benefited, especially when it comes to negotiations or visiting remote regions not easily reached by commercial flights.

1.3 Birth and development of private aviation

The private jet business began in the 1960s, when it was decided to combine engineering skill with customer satisfaction. The first jet custom-built for a customer occurred in 1964 and was the American Learjet 23, which offered speed and privacy, laying the foundation for the construction of its successors.

The greatest steps forward in terms of technology and expansion of flight capabilities occurred in the 1970s, with the advent of the turbofan engine, and in the 1980s, with the birth of the Gulfstream III, the first jet capable of making intercontinental crossings.

Between the 1990s and the 2000s, the desire for luxury and customisation contributed to the diversification of the various aircraft and the growth of sales, which continue to increase to this day. What drives investment in private jets is their stability and maintenance of value, and in the years of the COVID-19 pandemic, having such a means of transport meant being able to move undisturbed without being subjected to commercial airlines' cuts in routes and schedules.

Figure 1.1 shows two graphs depicting Business Jet sales from 2008 to 2012 and from 2012 to 2023. The first shows how, following the 2008 Financial Crisis, many of those who already

owned private jets decided to sell, but once the situation had settled down, the production and sale of new jets picked up again and did not stop, confining resale to a small portion of the market.

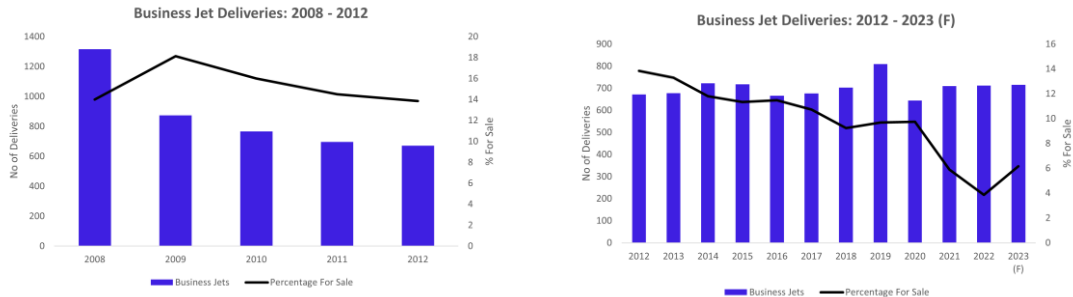


Figure 1.1: Business Jet Sales 2008 to 2023

This can be explained by considering that post-pandemic there was an influx of new buyers into the market for new jets, since, for the reasons explained above, there was a rush to lease business jets, which found agencies, whose availability of aircraft was limited, unprepared. This situation prompted both the agencies and the private user to purchase new aircraft.

The market for new jets subsided in 2022 due to factors such as economic concerns, rising operating costs, first and foremost fuel, and the inability to have the finished product in a short timeframe; rental agencies also did not feel compelled to buy as commercial airlines resumed full pace.

1.4 Future trends

The large number of new buyers entering the market in 2020 has expanded the customer base for new jets; it is estimated that half of these could become repeat customers, while a not insignificant number of older customers will return to invest in larger, more powerful and comfortable jets in line with their new needs.

In general, the surveys reveal optimism in the business jet community, as a large chunk of customers indicated plans to purchase aircraft in line with pre-COVID levels, pointing to a dynamic period for the business. Forecast International predicts that 7875 Business Jets will be produced in the decade 2023-2032, with a total value of USD 258.7 billion. It is estimated that annual Business Jet production will go from being the same as in 2023 (693 aircraft), to reach peaks of 863 aircraft in 2029, and then recover to slightly lower numbers around 775 aircraft.

The study also predicts which manufacturers will benefit the most, and these include all those manufacturers that will specialise in larger and more expensive aircraft.

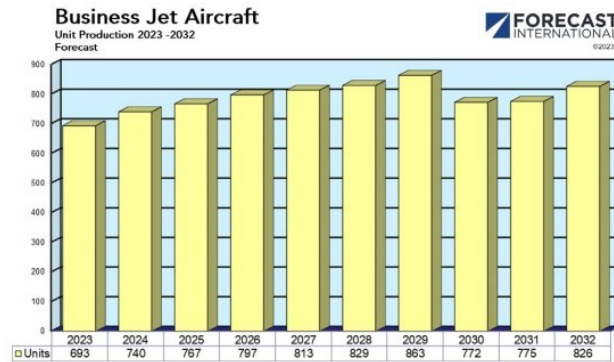


Figure 1.2: Business Jet Market Forecast by Forecast International

1.5 Environmental Impact of Business Jets

It is estimated that civil aviation accounts for 3% of global emissions, and a portion of this percentage is covered by private jets. Leaving aside the fact that there is a large disparity between the emissions of developing and developed countries, the average annual footprint per person is estimated to be around 4.7 tonnes in 2019. Taking this result and comparing it with the typical emissions of a private jet, which amount to tens of tonnes per flight and for a few passengers, one can get an insight into the inequality of emissions due to this mode of transport.

Currently, there is little or no research on this category of aircraft, as the main flight data providers, such as FlightRadar24 or FlightAware, offer their owners the option of removing them from the list. It is therefore necessary to resort to non-profit networks, such as OpenSky Network and ADS-B Exchange, in order to gain access to the data transmitted by each aircraft's ASD-B (Automatic Depend Surveillance - Broadcast): most private jets, in fact, are required to constantly transmit position, altitude and speed data for safety and air traffic management purposes.

Researchers at the TU Delft have used the datasets provided by OpenSky, cross-referenced with other sources such as socialnetworks, to define the typical trajectories and missions of 250 private jets, belonging to companies or prominent personalities, in order to assess their emissions in the time window that includes the years from January 2019 to October 2022. Among the most commonly used aircraft is the Gulfstream G650 (GLF6), so the study relied on its performance to also model the emissions of other, less common aircraft.

Many countries grant anonymity to owners of private jets, so linking the transponder code of the aircraft to its owners is difficult: social media has made the task easier, as jet owners often document their movements by posting them on their social profiles.

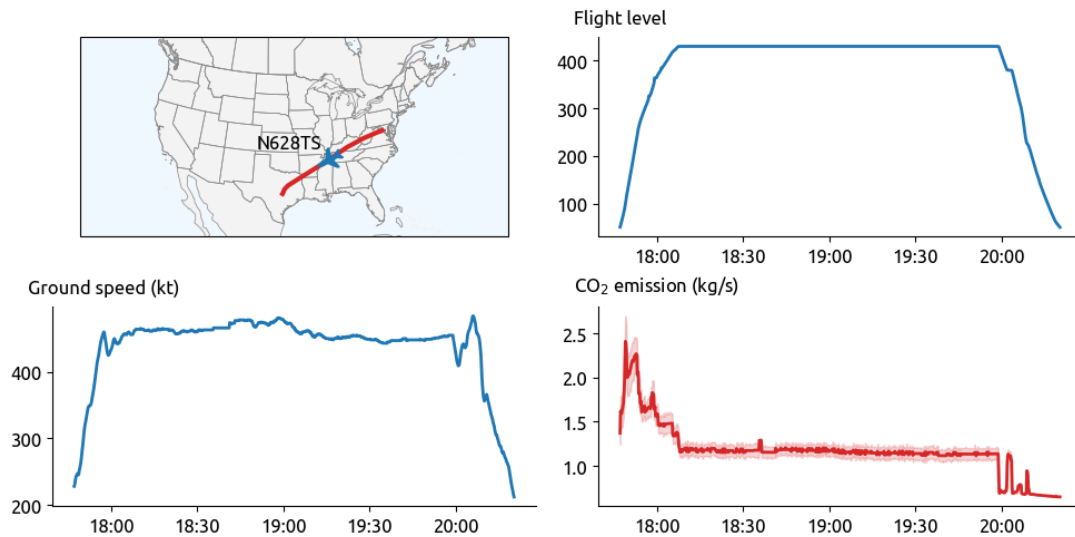


Figure 1.3: Example of a GLF6 flight and estimation of its CO₂ emissions

The total emissions of these aircraft are estimated to be between 0.45 and 0.5 megatonnes, and the annual average is the equivalent of the average emissions of about 45,000 people globally. The emissions are correlated with the distances travelled and the type of owner (private, corporate or both), but it should be noted that the time window considered also includes the year 2020, during which the COVID-19 pandemic inhibited the use of private jets. For this reason, the values found are underestimated compared to those that would be obtained by considering a year of normal aircraft use; another factor causing an underestimation of the results are the sanctions imposed on Russia following the invasion of Ukraine, which had a negative impact on the use of Russian private jets.

On average, in the pre-pandemic year 2019, jets emitted around 15 kilotonnes of per month, a figure that was equalled and exceeded in the post-pandemic year 2021. Interestingly, although almost the entire world population was forced into isolation in the year 2020, some private jets continued to fly.



Figure 1.4: CO₂ emissions of 250 private jets between 2019 and 2022

It should be noted that the model used has limitations, which can lead to under- or over-estimation- of the results found. These include the difficulty of establishing aircraft ownership over time, as, for example, some small airlines, which do not necessarily use jets, often purchase transponder codes from previous private aircraft: this could lead to an overestimation of emissions. Other problems are due to the limitations of OpenSky, which does not cover certain regions of the globe, such as Asia and the Middle East, both of which are home to many private jet owners: in this case, an underestimation occurs.

1.6 Categories

There are five main categories of business jets, the main characteristics of which are summarised in Table 1.1.

- *Very light jets*: They offer an alternative to turboprop aircraft, which are smaller and noisier. They are cheaper to operate than the next category, the Light Business Jets, have a lower weight and allow landing on shorter runways and smaller airports. They are the epitome of turboprop aircraft effectiveness and efficiency, but have about the performance of a light business jet.
- *Light business jets*: Although they are larger than VLJs, they still manage to land on short runways and at small airports. Most of these jets cannot accommodate a flight attendant.
- *Midsized business jets*: They can accommodate a larger number of passengers than the previous two categories, or alternatively, they accommodate the same number of passengers for the benefit of luxury and comfort, thanks to their larger spaces. They have autonomies that allow them to handle short to long-haul flights, even providing transcontinental flights. Generally, there is room to accommodate a flight attendant as

well. Compared to heavier jets, they are cheaper and still manage to land at small airports.

- *Super midsize business jets*: They boast a greater range, size and functionality than most midsize jets. Compared to the latter, they have a more spacious fuselage and improved avionics and enable them to cover larger ranges in a relatively short time.
- *Large business jets and heavy bizliner jets*: They boast extremely luxurious and spacious cabins. The crew can accommodate two flight attendants, and additional items not strictly necessary for flight activity. Some of them sacrifice their ability to reach great distances in favour of greater comfort. They reach the highest speeds of all categories.



Figure 1.5: Business Jet categories

Typology	Passengers	Range [km]	Cruise speed [km/h]
<i>Very light jet</i>	4-6	1610	772.5
<i>Light business jet</i>	5-6	2415	643.7-724.2
<i>Midsize business jet</i>	5-10	3219-4828	692.0-772.5
<i>Super midsize business jet</i>	8-10	5472-5794	1764-2124
<i>Large business jet and heavy (bizliner) jet</i>	10-18	>9565	772.5-2016

Table 1.1: Business Jet categories

1.7 Development and purpose of the thesis

The need to draft regulations covering the negative aspects of civil aviation became a serious concern in the early 1960s, with the introduction of the first generation of jet aircraft and the increase in their use in international flights. The Study Group on Aircraft Engine Emissions was established in 1973 as part of ICAO's Environmental Action Programme. The Committee on Aircraft Engine Emissions (CAEE) was subsequently set up in 1977 by the ICAO Council with the aim of developing specific standards for aircraft engine emissions; these Standards, adopted in 1981, set limits for the emission of smoke and certain gaseous pollutants for large turbojet and turbofan engines in future production; they also prohibit the venting of raw fuels. The scope of the existing Annex 16 was therefore extended to include provisions on engine emissions and the document was renamed Environmental Protection. Volume I of the reorganised Annex 16 contains provisions on aircraft noise, while Volume II contains provisions on aircraft engine emissions. ICAO has also developed several guidance manuals on noise and emissions.

In 2010, a collective action among countries around the world - developed and developing - to limit and reduce carbon emissions from international aviation, the State Action Plan on Reducing CO₂ Emissions from Aviation, was established. This initiative allows all ICAO member states to voluntarily establish a long-term climate change strategy for the international aviation sector.

On 6 March 2017, the ICAO Council of 36 States adopted a new standard on aircraft CO₂ emissions that will reduce the impact of aviation's greenhouse gas emissions on the global climate. Contained in the new Volume III of *Annex 16* to the Chicago Convention, the measurement of aircraft CO₂ emissions is the first global design certification standard regulating CO₂ emissions for any industry sector. The standard applies to new aircraft type designs from 2020 and to aircraft type designs already in production from 2023. Aircraft in production that do not meet the Standard by 2028 may no longer be produced unless their designs are sufficiently modified.

Of the four volumes of which the Standard is composed, it is of interest for this thesis to consider *Volume III, 'Aeroplane CO₂ Emissions'*.

In this thesis, a case study is chosen, attributed to the Business Jet category, and its aerodynamics and propulsion are studied, in order to obtain a sufficiently large database, which allows a plausible mission analysis to be carried out. Once the mission analysis has been carried out, all the necessary data is available to apply the current regulation on CO₂ emissions, provided by the ICAO, *Annex 16 - Volume III, 'CO₂ Certification Requirements'*, of 2017;

the aim of the thesis is to understand whether the current regulation for commercial aircraft is still applicable to business jets, or whether adjustments need to be introduced to adapt it to this category.

The case study is based on the Falcon 10 X aircraft of the French company Dassault, whose parts are currently in production, and will be delivered from the end of 2027, once certification is obtained. In order to obtain the aerodynamic database, it was necessary to take advantage of a CAD of a similar aircraft, so that it could be entered into the appropriate calculation programme and the various aerodynamic analyses could be carried out. The mesh on the aircraft was created using the ICEM CFD programme, after which the analyses were carried out using the Fluent Ansys programme.

The engine that will be mounted on the Falcon 10 X is the Pearl 10 X from the Rolls-Royce company, which is currently being certified. Once again, there was little data available, so the propulsion database was obtained using a Matlab calculation code, into which parameters were entered, chosen arbitrarily from certain ranges proposed in the literature. The result is therefore an approximation.

The mission analysis was carried out with the help of the ASTOS programme, from which it was possible to obtain the trend of various quantities, throughout the duration of the mission. The quantities useful in the calculation of the CO₂ metric were carefully chosen, and from them the quantities to be entered into the equations proposed by the ICAO regulations were extrapolated and implemented in a Matlab code.

Capitolo 2

CASE STUDY DESCRIPTION

Chapter 2 introduces the reference aircraft: the Falcon 10 X business jet of the French company Dassault Aviation. The main characteristics of the aircraft are described, such as configuration, size, performance and type of mission. Since the final aircraft is not yet on the market, to carry out this thesis it was necessary to consider an aircraft that fairly closely mirrors the Falcon 10 X, therefore the dimensions, technical specifications and CAD model of the reference aircraft are the result of a Conceptual Design.

2.1 Description of Falcon 10 X

The Falcon 10 X aircraft will join the French company Dassault Aviation's Business Jet family from 2027. The new jet's category is the ultra-long-range Business Jet; it has a wide-body and twin-engine configuration, with thrusters located in the tail and attached to the fuselage; the wing attachment is low and the tailplane is T-shaped. The aircraft will be equipped with 38 extra-large windows, 50% larger than that of the Falcon 8 X. The jet's structure will be constructed mostly of carbon-fibre composite, a material used for the fuselage, wing, and empennage, to ensure low weight and high structural strength.



Figure 2.1: Falcon 10 X

2.1.1 Dimensions

The aircraft dimensions are presented in Table 2.1 and are those declared by the manufacturer Dassault. From the values reported, it can be seen that the considerable dimensions of the aircraft will allow greater space and comfort than other jets in the same category; other advantages linked to the design choices are the modularity of the cabin, useful to guarantee greater freedom in the arrangement of the internal elements, according to the customer's requests.

<i>Fuselage length [m]</i>	33.40
<i>Aircraft hight [m]</i>	8.41
<i>Cabin length [m]</i>	16.46
<i>Cabin highth [m]</i>	2.03
<i>Cabin diameter [m]</i>	2.77
<i>Cabin volume [m³]</i>	78.72
<i>Cargo volume [m³]</i>	5.61
<i>Wingspan [m]</i>	33.63
<i>Wing surface [m²]</i>	122.78

Table 2.1: Falcon 10 X dimensions

2.1.2 Performance data

The performance data of the Falcon 10 X are shown in Table 2.2. With a range of 7,500 nautical miles, the Falcon 10X will nonstop connect opposite points on the globe. The maximum speed will be Mach 0.925, achieved through a combination of innovations in both structure and thruster design. The wing is characterised by high aspect ratios and sweep angles that increase the load-bearing capacity of the aircraft; it is equipped with movable surfaces such as flaps and four slats that allow better manoeuvrability and stability, especially at low speeds and on approach. All this is aided by the chosen material, carbon fibre composite, which allows minimal thicknesses and therefore less aerodynamic drag. The latter benefits not only attainable speeds, but also fuel consumption. The aircraft performance specifications are presented in Table 2.2 and are those declared by the manufacturer Dassault.

<i>Passengers</i>	19
<i>Crew members</i>	4
<i>Range [km]</i>	13890
<i>Maximum Mach</i>	0.925

<i>Cruise Mach</i>	0.85
<i>Maximum certified altitude [m]</i>	15545
<i>Take-off distance [m]</i>	<1829
<i>Landing distance [m]</i>	<262
<i>MTOM [kg]</i>	52163
<i>Max fuel weighth [kg]</i>	23451
<i>Maximum zero fuel weighth [kg]</i>	27805
<i>Payload [kg]</i>	2530

Table 2.2: Falcon 10 X performance data

2.1.3 Engines and avionics

The Falcon 10 X is equipped with two Rolls-Royce Pearl 10 X engines; the engine has so far clocked up 1,000 hours of testing to prove its reliability, performance requirements and compatibility with sustainable fuels (SAF). So far, the engine has proven to produce low combustion emissions, as well as low noise emissions.

The Pearl 10 X delivers a thrust of 18250 lbf, thanks to a 10-stage high-pressure compressor, a blisked fan with titanium vanes, an ultra-low emission combustor, a two-stage high-pressure turbine and a four-stage low-pressure turbine. Inside the powerplant, the Advance2 core, also invented by Rolls-Royce, provides a 5% increase in SFC compared to its predecessors, also fitted to corporate jets.

A gain in weight has been achieved by exploiting blisked technology, which consists of having a fan consisting of the rotor disc and vanes joined together to form a single piece; the vanes, therefore, cannot be disassembled and this gain in the number of parts to be used for assembly, combined with the type of material chosen (titanium), makes for a lighter fan. This technology is achievable through the use of high-level Additive Manufacturing techniques, which also help the structural strength of the part. The engine specifications are presented in Table 2.3 and are those declared by the manufacturer Rolls Royce.

<i>Engines</i>	2 x Rolls-Royce Pearl 10 X
<i>Thrust [kN]</i>	>80.1
<i>Avionics</i>	Next-generation NeXus Flight Deck with all Multi-Touch Displays

Table 2.3: Falcon 10 X engines and avionics data

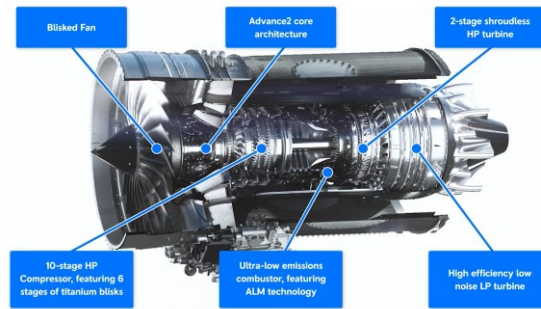


Figure 2.2:Rolls-Royce Pearl 10 X

2.1.4 Mission type

Table 2.4 shows the connections between airports that the Falcon 10 X will be able to make, without stopovers and with a single refuelling, to be carried out before take-off. The cities listed host airports that will actually be able to accommodate the aircraft, since requirements such as runway length are met:

- EZE: Ministro Pistarini International Airport, Buenos Aires, Argentina.
- CPT: Cape Town International Airport, Cape Town, South Africa.
- DXB: Dubai International Airport, Dubai, United Arab Emirates.
- GVA: Aéroport International de Genève, Geneva, Switzerland.
- HKG: Hong Kong International Airport, Hong Kong.
- JED: King Abdulaziz International Airport, Jeddah, Saudi Arabia.
- LOS: Murtala Muhammed International Airport, Lagos, Nigeria.
- LCY: London City Airport, London, UK.
- LAX: Los Angeles International Airport, Los Angeles, United States.
- MIA: Miami International Airport, Miami, United States.
- BOM: Chhatrapati Shivaji International Airport, Mumbai, India.
- GRU: Sao Paulo-Guarulhos International Airport, Sao Paulo, Brazil.
- SEA: Seattle-Tacoma International Airport, Seattle, United States.
- PVG: Shanghai-Pudong International Airport, Shanghai, China.
- SIN: Singapore-Changi Airport, Singapore.
- SYD: Kingsford Smith International Airport, Sydney, Australia.
- JFK: John Fitzgerald Kennedy International Airport, New York, USA.
- HND: Tokyo-Haneda Airport, Tokyo, Japan.

	E Z E	C P T	D X B	G V A	H K G	J E D	L O S	L C Y	L A X	M I A	B O M	G R U	S E A	P V G	S I N	S Y D	J F K	H N D
E Z E	X																	
C P T		X																
D X B			X															
G V A				X														
H K G					X													
J E D						X												
L O S							X											
L C Y								X										
L A X									X									
M I A										X								

out. For this purpose, data was collected from a *conceptual design* study for the Falcon 10X-like aircraft, which was done for teaching purposes.

The aircraft and mission requirements, from which the Conceptual Design was derived, are presented in Table 2.5.

<i>Payload [kg]</i>	110 x 22 passengers
<i>Maximum Cruise Mach</i>	0.925
<i>Maximum Cruise Altitude [m]</i>	15500
<i>Take off distance [m]</i>	1800
<i>Landing distance [m]</i>	1300
<i>Fuselage length [m]</i>	33.4

Table 2.5: Requirements

2.2.2 Wing and fuselage geometry

Since cruising is carried out at high speeds, it was necessary to choose a low taper ratio and high sweep angle to prevent shockwaves from forming on the wing and to reduce induced drag; with this arrangement, in fact, the speed seen by a swept wing is lower than what a non-swept wing would see, so the critical Mach number is higher. To further stabilise the aircraft, it was given a dihedral angle. All inputs to obtain the wing geometry are summarised in Table 2.6.

<i>Taper ratio</i>	0.17
<i>Sweep angle [deg]</i>	37.0
<i>Dihedral angle [deg]</i>	2.50
<i>Distance fuselage top - wing leading edge [m]</i>	12.0
<i>Fuselage diameter [m]</i>	3.00

Table 2.6: Inputs for wing design

As outputs the values in Table 2.7 were obtained.

<i>Wing area [m²]</i>	119.2
<i>Wing span [m]</i>	36.6
<i>Aspect ratio</i>	9.50
<i>Root chord [m]</i>	6.05
<i>Mean chord [m]</i>	3.54
<i>Tip chord [m]</i>	1.03

Table 2.7: Outputs for wing design

The airfoil chosen is the NASA SC-0610, supercritical, with a t/c of 0.1.

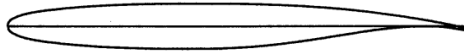


Figure 2.3: NASA SC-0610

The length of the fuselage and its diameter are inputs, the former was taken equal to that provided by the aircraft manufacturer, the latter was calculated from the diameter of the cabin, again declared by Dassault, adding about 20 cm, to take into account a wall thickness of about 10 cm. The fuselage section is circular.

Fuselage length [m]	33.4
Fuselage diameter [m]	3.00

Table 2.8: Fuselage geometry

2.2.3 Tail geometry

The vertical tail is not tapered, but has a swept angle. A connection between this element and the tail cone of the fuselage was not considered at this design stage, but in more advanced stages of the structural analysis it will have to be provided in order to ensure a better distribution of stresses. The geometric characteristics of the vertical tail are presented in Table 2.9.

Vertical tail length [m]	5.13
Root chord [m]	4.00
Tip chord [m]	4.00
Sweep angle [deg]	40.0

Table 2.9: Vertical tail geometry

The horizontal tail was positioned 31.5 m from the longitudinal axis of the fuselage in the vertical direction and 6 m in the horizontal direction; the positioning was chosen from considerations of the sweep angle of the vertical tail. There is no dihedral angle, but there is a sweep angle. The geometric characteristics of the vertical tail are presented in Table 2.10.

Horizontal tail length [m]	11.2
Root chord [m]	3.30
Tip chord [m]	1.80
Sweep angle [deg]	34.0

Table 2.10: Horizontal tail geometry

For both the vertical tail and the horizontal tail, the NACA 0010 profile was chosen, having a t/c ratio of 0.1.



Figure 2.4: NACA 0010

2.2.4 CAD model

Considering the geometric characteristics obtained and the design choices made, a CAD model of the aircraft was obtained using Solidworks software, of which three views are presented in Figure 2.5, one frontal, one lateral and one top view, accompanied by dimensions; this model is the one used to perform the aerodynamic analysis presented in Chapter 4.

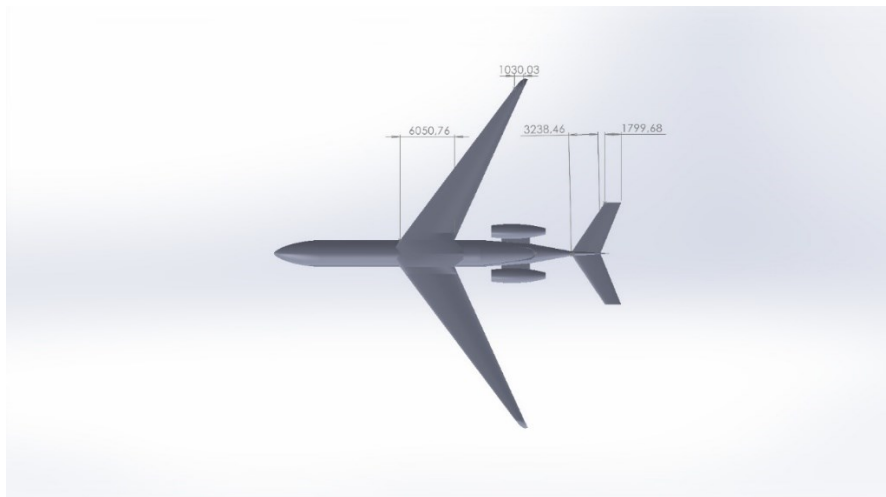
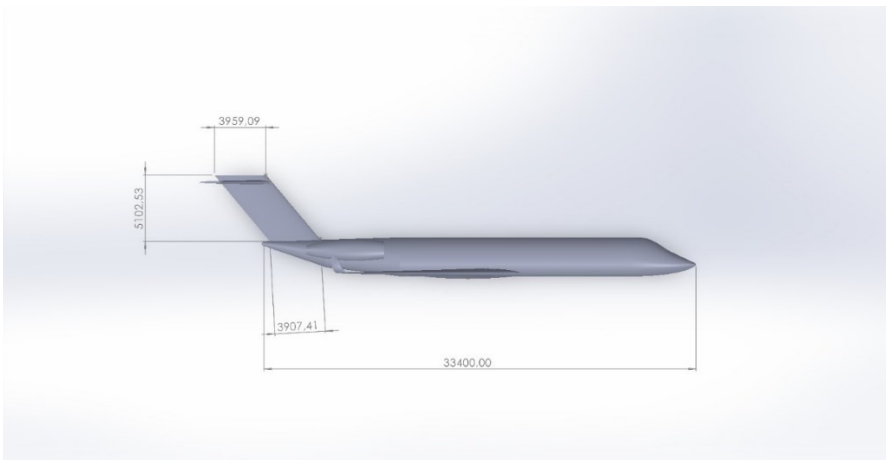
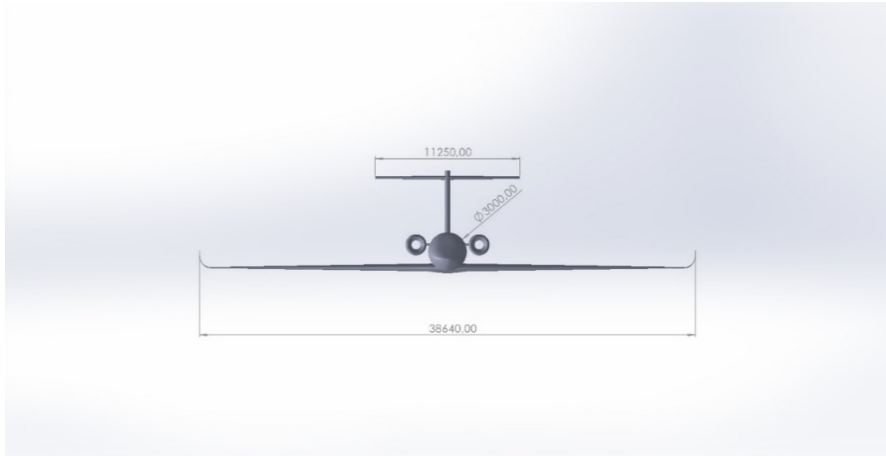


Figure 2.5: CAD and dimensions – 1 frontal view, 2 lateral view, 3 top view

Capitolo 3

CO₂ METRIC VALUE ACQUISITION– LOW-FIDELITY ANALYSIS

In Chapter 3, all the steps taken to arrive at the calculation of the CO₂ metric value are discussed in detail in order to realize a *low fidelity analysis* that starts from an aerodynamic simulation, based on Raymer's model. Subsequently, the propulsion system was simulated using the Mattingly equations. The Chapter ends with the calculation proposed in *Annex 16 – Volume 3, “CO₂ Certification Requirements”*.

3.1 Aerodynamics simulation

3.1.1 Aerodynamic forces

This section delves into the complexity of aerodynamic analysis, breaking it down into various parameters and coefficients, often leading to confusion with the different types of lift and drag. These terms are considered "accounting fictions," created to simplify calculations, but they don't directly represent the actual physics of airflow over an aircraft.

As the aircraft moves forward, air molecules move across its surface. Those closest to the skin adhere to it (no-slip condition), creating a shear layer between them and the stationary air molecules farther away. This phenomenon, caused by air's viscosity (its drag to shear), generates skin-friction drag. When airflow is smooth, it's called *laminar*, but when it becomes disorganized, it's "turbulent," leading to a thicker boundary layer and increased drag. Airflow transitions to turbulence when the Reynolds number reaches about 500,000, but this can happen sooner if the surface is rough or curved. The chapter explains how changes in air velocity around the aircraft affect pressure, with Bernoulli's equation showing that when velocity increases, static pressure decreases, and vice versa.

Lift is produced by a pressure differential created when air moves faster over the top of the wing than beneath it, driven by the wing's angle of attack or camber. Ultimately, only two

forces act between the airplane and air: friction (tangential) and pressure (perpendicular). All aerodynamic coefficients are simply different combinations of these two forces.

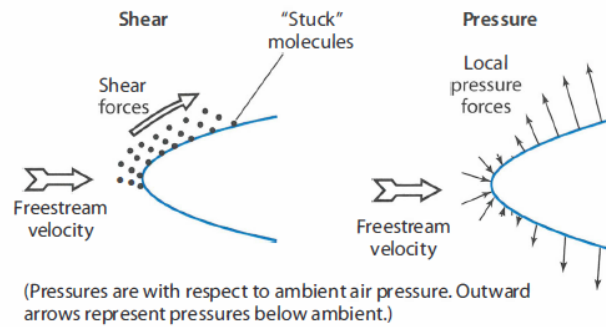


Figure 3.1: Origin of aerodynamic forces

Considering the drag, it includes different terms like skin-friction drag, parasite drag, wave drag, and more, for example, at supersonic speeds, shock waves create additional pressure forces that contribute to drag. Parasite drag (or zero-lift drag) is largely composed of skin-friction drag, which depends on the aircraft's wetted area. However, additional pressure drag, such as boattail drag caused by separation of airflow near the rear of the aircraft, also plays a role. Form drag (viscous separation drag) occurs when airflow separates from the aircraft surface, resulting in pressure differences that create drag. Other forms of drag include scrubbing drag, caused by jet exhaust or propwash increasing skin-friction drag, and wave drag, which occurs at high subsonic and supersonic speeds due to shock formation. Wave drag is a function of both the shape of the aircraft and its lift. Drag due to lift, such as induced drag, occurs as a result of the energy required to generate lift and is proportional to the square of the lift. Induced drag is a subset of the overall drag related to lift, and its estimation is a key part of aerodynamic analysis.

3.1.2 Aerodynamic coefficients

Lift and drag can be defined as a product of their nondimensional coefficients, the *dynamic pressure*, q , expressed by the Bernoulli's theorem, and the *wing reference area*, S , that is the full trapezoidal area extending to the aircraft centerline.

$$L = qSC_L$$

$$D = qSC_D$$

Where

$$q = \frac{1}{2} \rho V^2$$

The lift force is perpendicular to the direction of the freestream speed, while the drag force is parallel to the direction of the freestream speed.

The lift coefficient can be expressed as a function of the angle of attack:

$$C_L = C_{L_0} + C_{L_\alpha} \cdot \alpha$$

Where C_{L_α} is the slope of the linear section of the $C_L - \alpha$ curve and depends on the Mach number and the flight regime. Since the airfoil studied is cambered, C_{L_0} is not zero, but the lift at zero angle of attack cannot be evaluated, so C_{L_0} is supposed to be zero as a first approximation.

For subsonic Mach numbers C_L can be evaluated by using a semi-empirical formula:

$$C_{L_\alpha} = \frac{2\pi \cdot AR}{2 + \sqrt{4 + \left(\frac{AR \cdot \beta}{\eta}\right)^2 \left(1 + \frac{\tan^2(\Lambda)}{\beta^2}\right)}} \left(\frac{S_{exposed}}{S_{ref}}\right) F$$

Where

$$\beta = 1 - M^2$$

$$\eta = 0.95$$

η is the airfoil efficiency and it's used to consider that actual airfoils have lift-curve slopes between about 90% to 100% of the theoretical value. AR is the aspect ratio of the wing that is reduced as the slope of the lift curve is reduced. $S_{exposed}$ is the exposed wing planform and F is the fuselage lift factor which considers the lift generated by the fuselage diameter d :

$$F = 1.07 \left(1 + \frac{d}{b}\right)^2$$

The product $(S_{exposed}/S_{ref})F$ is greater than one, implying that the fuselage produces more lift than the portion of the wing it covers, that is unlikely, so it's set to 0.98. The lift coefficient was calculated for multiple angles of attack, covering a range from -5.1 degrees to 10 degrees.

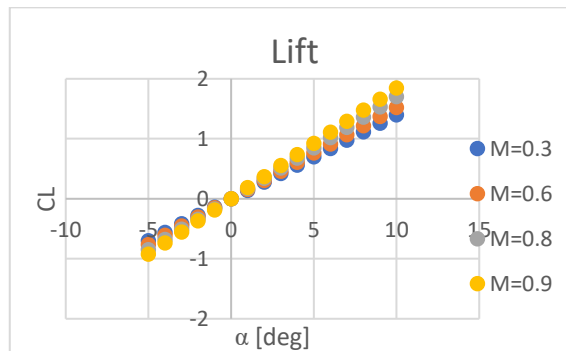


Figure 3.2: Lift - Raymer model

The drag coefficient can be written as the sum of two contributions: the zero lift drag coefficient C_{D_0} - given by the sum of skin friction drag coefficient C_{D_f} , the miscellaneous drag coefficient $C_{D_{misc}}$ and the leakage and protuberance drag coefficient $C_{D_{L\&P}}$ - and C_{D_i} .

$$C_D = C_{D_0} + C_{D_i}$$

The zero lift drag coefficient is

$$C_{D_0} = \frac{\sum(C_{f_c} \cdot FF_c \cdot Q_c \cdot S_{wet_c})}{S_{ref}} + C_{D_{misc}} + C_{D_{L\&P}}$$

Where C_{f_c} is the flat plate skin-friction, FF_c is a form factor which takes in account the component's pressure drag due to viscous separation, Q_c is a factor which considers any interference effects on the component drag and S_{wet} is the wetted area of each element. The miscellaneous drag $C_{D_{misc}}$ includes the drag produced by the special features of an aircraft (like flaps, unretracted landing gear, etc.).

Since a laminar flow is considered, the skin-friction coefficient can be evaluated as:

$$C_f = \frac{1.328}{\sqrt{Re}}$$

Where Re is the Reynolds number, which expresses the influence of viscous and inertial effects on flow:

$$Re = \frac{\rho VL}{\mu}$$

The form factor FF_c is an empirical correction and allows to consider the effect of flow separation on pressure drag; there is a form factor for each element of the aircraft, shown in Table 3.1.

Component	FF
Wing	$\left[1 + \frac{0.6}{\left(\frac{x}{c}\right)_{max} \left(\frac{t}{c}\right) + 100 \left(\frac{t}{c}\right)^4} \right] \cdot 1.34 \cdot M^{0.18} (\cos\Lambda)^{0.28}$
Fuselage	$0.9 + \frac{5}{f^{1.5}} + \frac{f}{400}$
Nacelle	$1 + \frac{0.35}{f}$

Table 3.1: FF calculation

Where $\left(\frac{x}{c}\right)_{max}$ is the chordwise location of the airfoil maximum thickness point, $\frac{t}{c}$ is the airfoil thickness to chord length ratio, Λ is the sweep angle of the wing and $f = \frac{l}{d}$.

The interference drag Q_c is evaluated depending on the element that is considered, as shown in Table 3.2.

<i>Component</i>	Q_c
<i>Fuselage</i>	1
<i>Wing</i>	1
<i>Nacelle</i>	1.5
<i>Tail surface</i>	1.03

Table 3.2: Q_c values

The induced drag C_{D_i} can be expressed proportional to the square of the lift coefficient at low angles of attack:

$$C_{D_i} = k \cdot C_L^2$$

Where k , at subsonic Mach number, can be written as:

$$k = \frac{1}{\pi \cdot AR \cdot e}$$

Since the wing swept angle is about 37° , the Oswald efficiency, due to a non-elliptical lift distribution and flow separation, is written as:

$$e = 4.61(1 - 0.045 \cdot AR^{0.68}) - (\cos\Lambda)^{0.15} - 0.31$$

The drag coefficient was calculated for multiple angles of attack, covering a range from -5.1 degrees to 10 degrees.

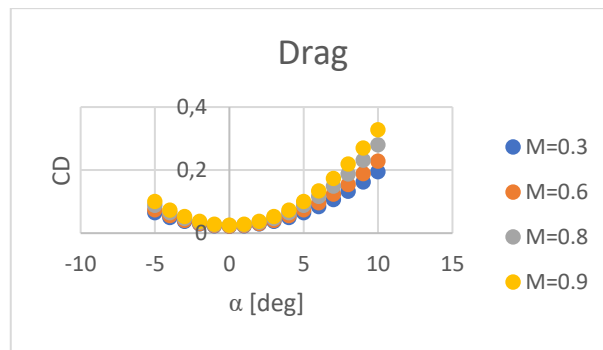


Figure 3.3: Drag - Raymer model

3.2 Simulation of the Propulsion System

3.2.1 On-design analysis

The type of power unit chosen follows the characteristics of the Pearl 10 X, which will actually be mounted on the Falcon 10 X once it is put on the market; a separate-flow turbofan was considered, the layout of which is illustrated in Figure 3.4.

From Figure 3.4, it is evident that the engine features a single inlet that divides, after passing through the compression fan, into a core (primary) stream and a bypass (secondary) stream. Notably, the bypass stream is not subjected to further compression, whereas the primary stream undergoes additional compression, followed by combustion and passage through two turbines. These turbines generate the power required for both the main compressor and the compression fan. Finally, the two streams are expelled through separate exhaust nozzles.

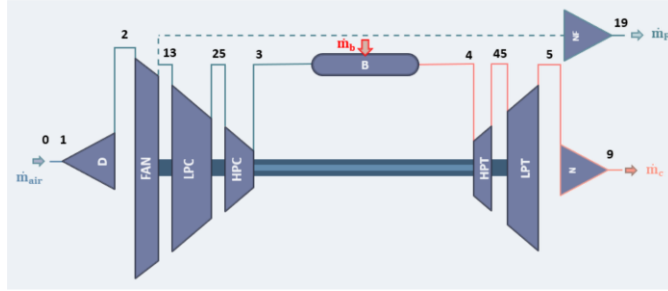


Figure 3.4: Turbofan scheme

An engine parametric cycle analysis can be run, by implementing equations and procedures proposed by Mattingly (1985), In order to obtain thruster performance, such as thrust and TSFC, design choices must be made and the flight environment defined, selecting certain parameters, presented in Table 3.3 together with the values established for them.

Cruise Mach was chosen from the technical specifications provided by the aircraft manufacturer, as well as the Cruise Altitude. The $\left(\frac{T}{W}\right)^*$ parameter was calculated by dividing the thrust (declared by the Pearl 10 X manufacturer) doubled and the MTOW, given by Dassault.

$$\left(\frac{T}{W}\right)^* = \frac{81180 \cdot 2}{52163 \cdot 9.81}$$

α and π_c were chosen according to the most common turbofan engines used in the business modern aviation.

h_{PR} is the typical value of HEFA 215, that is a type of bio-derived jet fuel produced using the Hydrotreated Esters and Fatty Acids (HEFA) process. This process involves refining various oils and fats, such as vegetable oils or waste fats, by treating them with hydrogen. The result is a sustainable aviation fuel (SAF) that is chemically similar to conventional jet fuel but has a reduced carbon footprint.

The value of throttle, expressed by the *Turbine Inlet Total Temperature*, has been chosen following the results of studies about performances high bypass ratio turbofan, for both on-design and off-design value.

Cruise Mach	0.85
Cruise Altitude [m]	15500
Thrust to Weight Ratio, $\left(\frac{T}{W}\right)^*$	0.317
Bypass ratio, α	5
Overall Pressure Ratio, π_c	50
Throttle, T_4° [K]	1336
Lowest calorific value of fuel, h_{PR} [J/kg]	43.7e6

Table 3.3: Requirements of the propulsion system

Il risultato generato dall'applicazione del ciclo parametrico è presentato nelle Figure 3.5, 3.6 e 3.7. Graphically, one can find the design point, described by the values of *Uninstalled Specific Thrust* and of *Uninstalled Specific Thrust Fuel Consumption* in Table 3.4.

Uninstalled Specific Thrust [kg/(kg/s)]	140.28
Uninstalled Specific Thrust Fuel Consumption [mg/N s]	17.20

Table 3.4: Performances on design point

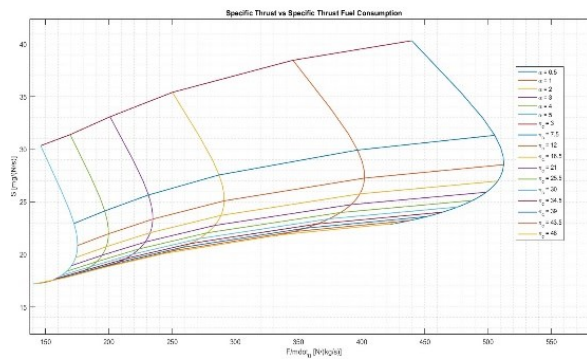


Figure 3.5: Specific Thrust vs Specific Thrust Fuel Consumption

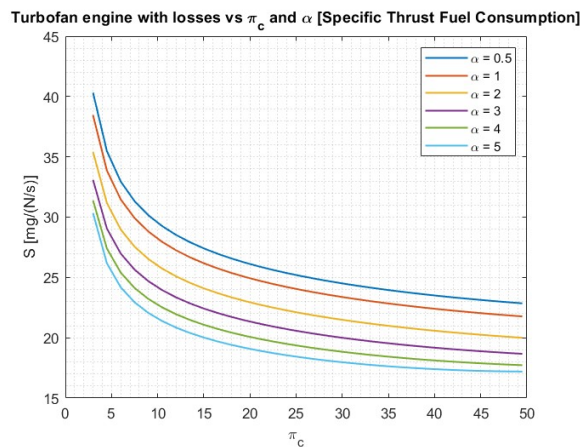


Figure 3.6: Turbofan engine with losses vs π_c and α

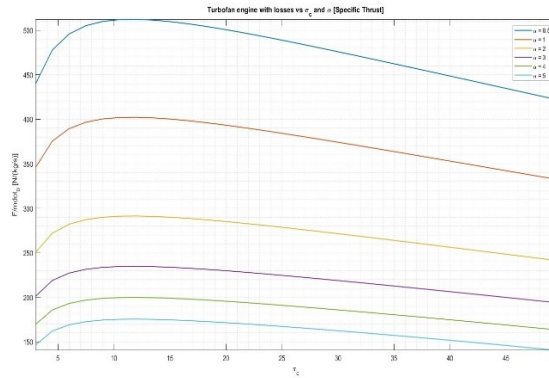


Figure 3.7: Turbofan engine with losses vs π_c and α

3.2.2 Off-design analysis

At this point, one can proceed with the analysis of the engine's performance, again applying the Mattingly equations. In order to evaluate the engine's behaviour under various operating conditions, four different Mach numbers were chosen and for each of which three throttle configurations were set. For each combination of Mach number and throttle, the analysis was carried out at 12 equispaced points of altitude, from 0 to 12000 m. Everything is summarised in Table 3.5 and the results of the analysis are presented in Figure 3.9.

Mach number	[0.3, 0.6, 0.8, 0.9]
Throttle [%]	[60%, 80%, 100%]
Altitude [m]	[0, 1091, 2182, 3273, 4364, 5455, 6545, 7636, 8727, 9818, 10909, 12000]

Table 3.5: Mach, Throttle and Altitude settings

The throttle is expressed in terms of the percentage of Turbine Inlet Temperature (T_{t_4}), choice of 1800°C, so about 2000 K, considering that at take-off the throttle is set to the maximum value and the trend of T/O's T_{t_4} is that presented in the graph in Figure 3.8.

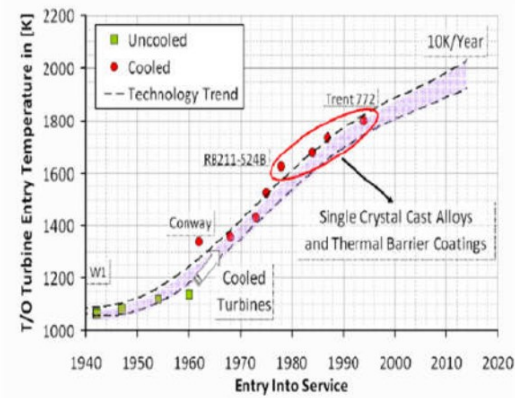


Figure 3.8: Evolution of turbine entry temperature and future trend (Kyprianidi 2011)

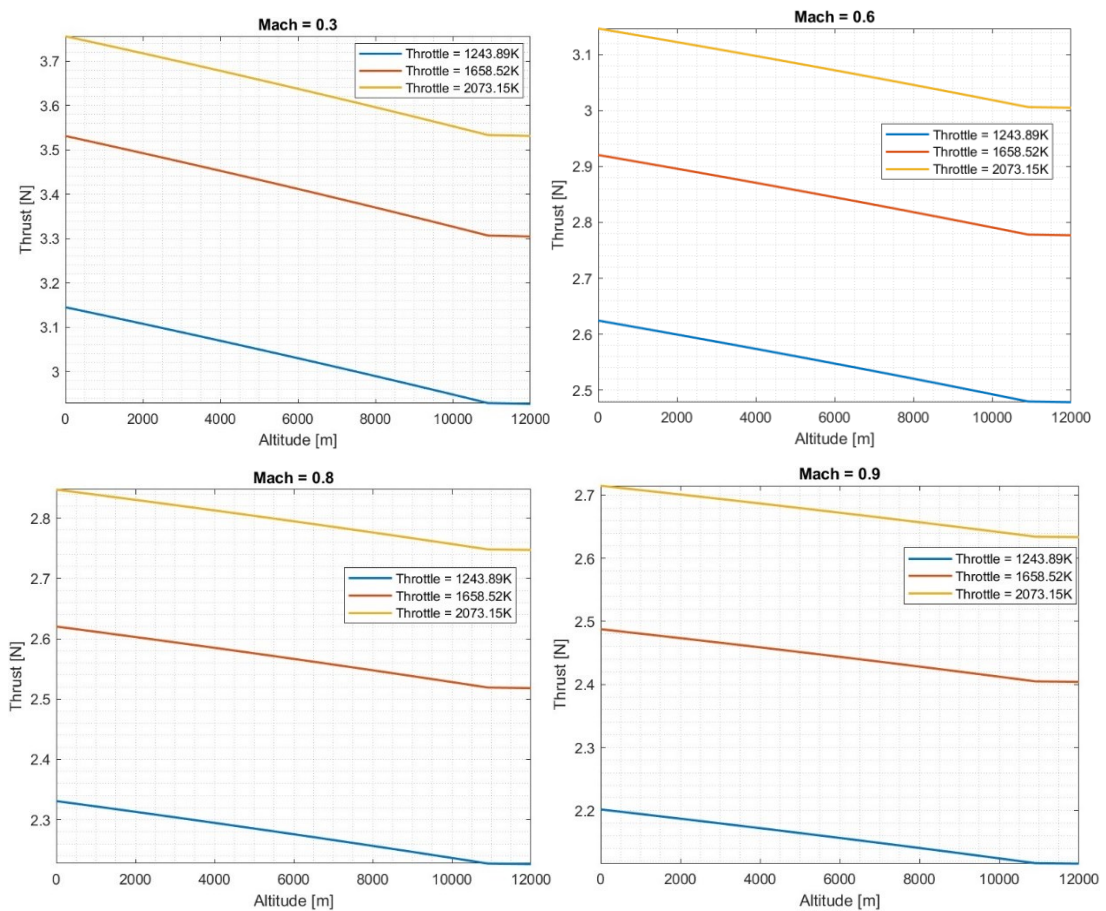


Figure 3.9: Thrust vs Altitude at different Mach numbers

Some of the most representative results per engine are presented in Table 3.7, where each phase is characterised by the configuration presented in Table 3.6.

Flight phase	Mach number	Throttle setting [%]	Altitude [m]
<i>Take-off</i>	0.3	1	0
<i>Landing</i>	0.3	0.6	0

<i>Cruise</i>	0.8	0.8	12000
<i>Maximum Mach Cruise</i>	0.9	1	12000

Table 3.6: Flight phases settings

Flight phase	T_{scal} [N]	T [N]	TSFC [kg/N s]	m_b[kg/s]
<i>Take-off</i>	37352	37560	1.1437e-05	0.44288
<i>Landing</i>	31448	31448	1.4598e-06	0.045908
<i>Cruise</i>	25182	99533	1.2879e-05	0.32433
<i>Maximum Mach Cruise</i>	26336	104094	1.9230e-05	0.50645

Table 3.7: Results of off-design analysis

3.3 Mission simulation

3.3.1 ASTOS - Advanced Simulation Tool for Space Operations

ASTOS (Advanced Simulation Tool for Space Operations) is an advanced software primarily used in the aerospace field for the planning, simulation, and optimization of space missions. This tool is developed to support engineers and operators in the design of flight trajectories, orbital maneuvers, and complex operations during space missions, both for satellites and interplanetary probes. The main goal of ASTOS is to provide a simulation environment that accurately models the conditions and constraints of a space mission, optimizing fuel consumption, mission duration, orbits, and necessary maneuvers.

3.3.2 Mission type

In the case under consideration, although we are not dealing with a vehicle capable of space missions, the software still allows for the input of data related to the aircraft under study and the simulation of a typical mission by combining the data provided by aerodynamics and propulsion. The aircraft is long-range, so the objective is to create a mission with a very long cruise, both in terms of time and distance. The mission will consist of the phases listed in Table 3.8.

Pre-flight check
Engine start-up
Taxi out
Take-off
Climb

Cruise
Descent
Approach
Landing
Taxi-in
Engine shutdown

Table 3.8: Flight phases

In general, these phases can be grouped into four sets:

- *Ground phases*: the simulation consists of pre-flight checks, which cover all aircraft preparations from a cold-and-dark state to engine start-up, followed by the taxi-out and taxi-in phases, where typical taxi times have been selected based on average airport conditions. The final stages include the runway run phases for take-off and landing, ensuring all necessary procedures and checks are performed for a smooth transition between each stage of the flight.
- *Climb*: the climb phase consists of the take-off rotation maneuver followed by the actual climb. The duration of the climb has been determined by considering a reasonable average climb rate of 1034 ft/min, with a higher climb rate at lower altitudes and a decreasing rate as the aircraft approaches the cruise altitude of 12000 meters.
- *Descent*: the approach phase begins with an average descent rate of -1034 ft/min, taking into account that the descent rate will be higher in the initial stages and decrease towards the end of the phase. During the approach, flaps and landing gear are deployed in preparation for the landing phase.
- *Cruise*: the cruise is performed at a constant altitude of about 12000 m and a speed of Mach that increases from 0.85 to 0.90.

The output of the simulation will be the mission profile, defined as altitude as a function of time, accompanied by graphs that represent other key variables for the final calculation, such as fuel flow and the variation of the Mach number.

3.3.3 Simulation setting

To simulate the aircraft's mission in ASTOS, the process begins with defining the mission environment, including the gravitational constant and the Earth's atmosphere, specifically the US Standard model.

Once the environment is characterized, the aircraft can be defined, particularly the engines, aerodynamics, and fuselage in the *Vehicle Parts and Properties section*. The engines are specified as Airbreathing, with Turbofan engines selected. After this, the axial thrust and fuel consumption must be configured. This is done by importing a CSV file into the “profile” section, containing various operational conditions, considering flight Mach, throttle setting, and altitude to provide thrust and fuel consumption data. The CSV file is provided by the simulation of the Propulsion System presented in the previous subparagraph. Additionally, a throttle setting was chosen, which can be adjusted later to manage different phases of the mission.

Subsequently, the aircraft’s aerodynamic is defined, beginning with setting the wing area and then the lift and drag coefficients data were imported through a CSV file that considers flight Mach and the aircraft’s angle of attack, obtained by the definition of a script, written with Python.

Lastly, it’s selected the liquid fuel. The structure’s weight and maximum fuel weight are also set in this phase.

Moving to the *Vehicles and POIs Definition* section allows the connection of engines to the fuselage tank, defining a core containing the two components. In the image, the aircraft does not correspond to the described one but serves as a graphical representation independent of the simulator’s input data.

With all parts defined, the mission definition can proceed, from take-off to landing. The methodology used for recreating the mission is *trial and error* defining various phases consecutively. In this case, the mission is divided into three different phases, since the Ground phases are not considered.

The phases are defined by varying the aerodynamic and throttle configurations, maintaining the other parameters constant.

The state type *Position and Velocity* is set, selecting the *PCPF* frame, with initial conditions of longitude, and latitude set to the 2.5 degrees and 49.01 degrees respectively and altitude set to zero meters. For the velocity, *Relative PCPF* frame and *L* representation are selected, with an initial velocity of 100 m/s, and zero inclination and heading.

3.3.4 Phase definition: Climb, Cruise, Approach

Up to this point, the aircraft and environment have been defined in as much detail as possible to ensure a reliable simulation. As previously mentioned, this section will focus on the control laws applied during different phases of the mission, which form the foundation of the simulation. Specifically, the discussion will concentrate on longitudinal dynamics, using

the angle of attack or pitch as the control variable; the other control variable is the throttle setting, expressed in percent of thrust. In this way it's possible to analyze how velocity, altitude, and fuel mass respond accordingly.

During the *Climb phase* a linear control law was maintained, using the *Euler Angles*, in particular the pitch angle, as the control variable; the range of angles considered goes from 5.00 to 6.00 degrees. The throttle was first set on 1. The phase duration is about 33 minutes.

The *Cruise phase* is the longest one, since it lasts about 16 hours at a constant altitude of 12000 m and a Mach number growing from 0.85 to 0.90. In this case the simulation was made by changing the *Aerodynamics Angles*, in particular the angle of attack, which was set on 5.00° at the beginning of the phase and gradually decreased to 1.33°. The throttle was initially set at 1.0, then lowered to 0.5.

The final phase, the *Approach* one, lasts 33 minutes and was still made by modifying the Euler angles, in particular the pitch one.

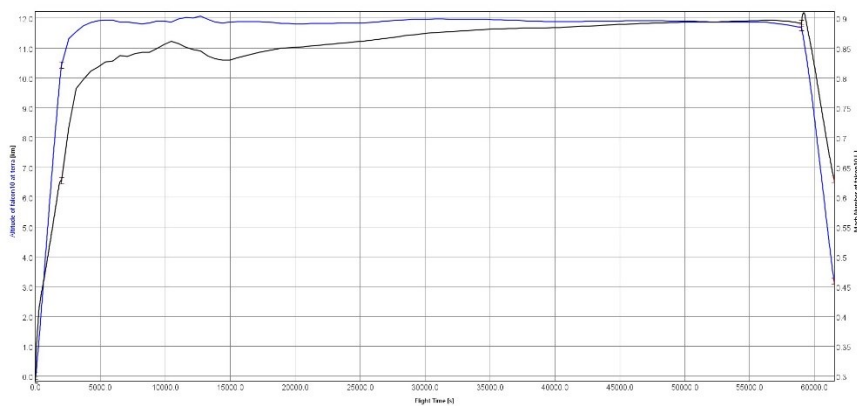


Figure 3.10: Altitude, Mach number vs time

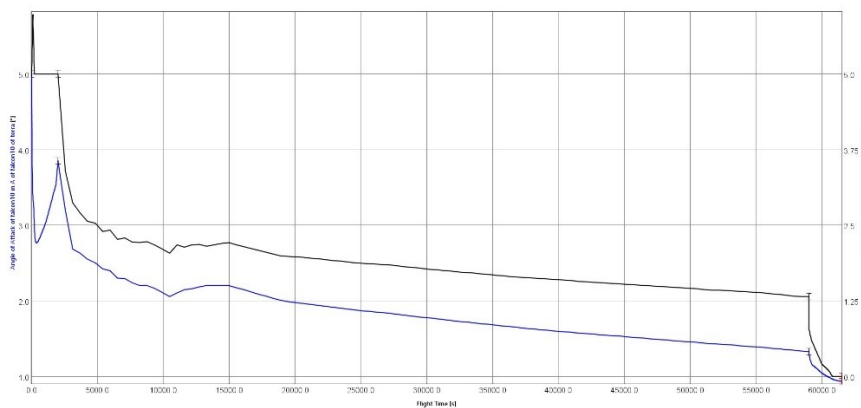


Figure 3.11: Angle of attack, pitch vs time

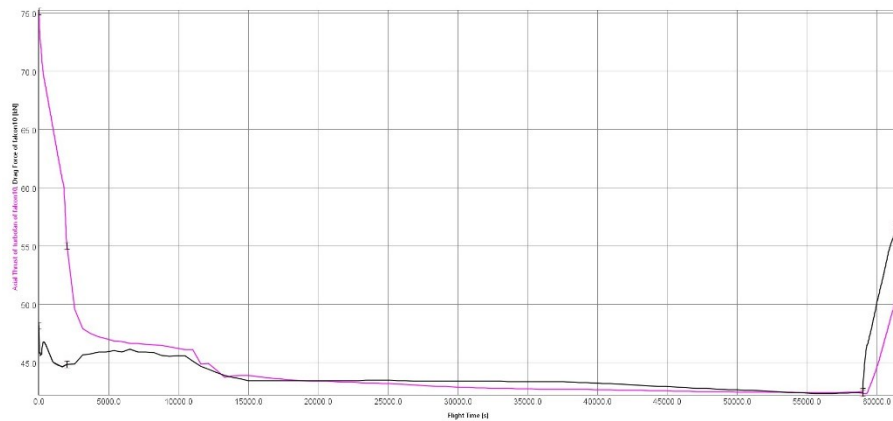


Figure 3.12: Thrust, drag force vs time

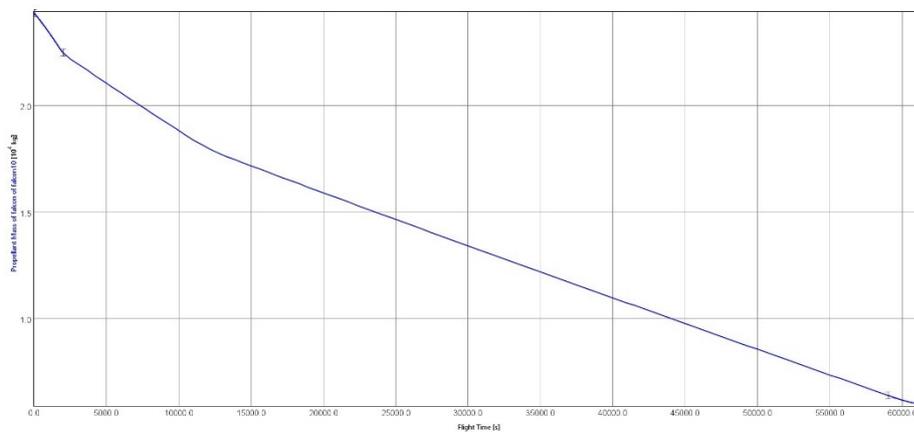


Figure 3.13: Propellant mass flow

3.4 Application of the standard

3.4.1 CO₂ metric value definition

In *Volume III of Annex 16*, there is a list of aircraft to which the standard applies. More specifically, to decide on the approach to defining the CO₂ metric value, the Falcon 10 X must be placed in a specific category chosen from those provided. The aircraft falls under category *b*), as described in *Chapter 2* of the document.

“b) subsonic jet aeroplanes, including their derived versions, of greater than 5 700 kg and less than or equal to 60 000 kg maximum take-off mass with a maximum passenger seating capacity of 19 seats or less, for which the application for a type certificate was submitted on or after 1 January 2023;” (Annex 16 – Volume III, Chapter 2, ICAO, 2017)

The CO₂ metric value is calculated using the formula provided in the document and is expressed in $[kg/km]$:

$$CO_2 \text{ metric value} = \frac{\left(\frac{1}{SAR}\right)_{AVG}}{RFG^{0.24}}$$

To calculate it, the values for *Specific Air Range (SAR)* and *Reference Geometric Factor (RFG)* must be defined. With the MTOM value available, the maximum and minimum permissible CO₂ metric values for category b) can be calculated (Annex 16 – Volume III, Chapter 2, ICAO, 2017).

$$\text{Maximum permitted } CO_2 \text{ value} = 10^{\left(-2.73780 + (0.681310 \cdot \log_{10} MTOM) + (-0.0277861 \cdot (\log_{10} MTOM)^2)\right)}$$

The obtained value is shown Table 3.9.

MTOM [kg]	52163
Maximum permitted CO₂ value [kg/km]	0.7209

Table 3.9: CO₂ maximum permitted metric value

3.4.2 SAR calculation

The document defines *Specific Air Range (SAR)* as:

$$SAR = \frac{TAS}{W_f}$$

Where *TAS* is the *True Airspeed* and *W_f* is the total mass flow of fuel. The parameter has to have the dimensions of [km/kg].

In order to calculate SAR, *gross masses* must be introduced. They are expressed in kg and defined as shown:

$$\text{high gross mass} = 0.92 \cdot MTOM$$

$$\text{low gross mass} = (0.45 \cdot MTOM) + (0.63 \cdot (MTOM)^{0.924})$$

$$\text{mid gross mass} = \text{average}(\text{high gross mass}, \text{low gross mass})$$

Taking into account the MTOM of the CAD model, it's possible obtaining the valued shown in Table 3.10:

MTOM [kg]	52163
High gross mass [kg]	47990
Low gross mass [kg]	37867
Mid gross mass [kg]	42929

Table 3.10: Gross masses

With the mission profile available, it is possible to visualize the altitude trend as a function of mass to see where the three gross masses are positioned. If the regulation were applied to an aircraft used in civil aviation, the three masses would correspond to the beginning, middle, and end of the cruise phase, respectively; the result is shown in Figure 3.14.

For the SAR calculation, ambient temperature (T) data at the altitudes reached during the mission were extracted from ASTOS, allowing the calculation of the speed of sound at each point considered:

$$a = \sqrt{\gamma RT}$$

Referring to the Standard Atmosphere, air is considered a mixture of diatomic gases, consisting of 79% molecular nitrogen (N₂) and 21% molecular oxygen (O₂); the value of the *adiabatic index* γ and the *universal gas constant* considered is presented in Table 3.11.

γ	1.4
R [J/kg · K]	287

Table 3.11: Air values for γ and R

With the speed of sound available and by exporting the Mach (M) data from ASTOS, the TAS can be derived:

$$TAS = M \cdot a$$

For the three notable points, the values shown in Table 3.12 are obtained. The fuel flow values were extracted from the mission profile using ASTOS.

	<i>T [K]</i>	<i>a [m/s]</i>	<i>M</i>	<i>TAS [m/s]</i>	<i>W_f [kg/s]</i>	<i>SAR [km/kg]</i>
<i>High gross mass</i>	216.65	295.04	0.8385	247.39	0.4466	553.96
<i>Low gross mass</i>	216.65	295.04	0.8910	262.89	0.2414	1089.1
<i>Mid gross mass</i>	216.65	295.04	0.8586	253.32	0.2496	1014.7

Table 3.12: SAR calculation: temperature, sound speed, Mach number, TAS, fuel mass flow, SAR

The SAR values as a function of mass are shown in Figure 3.7. At this point, the inverse of each individual value obtained must be taken, and their arithmetic mean calculated; the resulting value will form the numerator of the formula for calculating the CO₂ metric value. The values obtained are presented in Table 3.13.

	<i>SAR [km/kg]</i>	<i>1/SAR [km/kg]</i>	$\left(\frac{1}{SAR}\right)_{AVG}$ [km/kg]
<i>High gross mass</i>	553.96	1.8052e-3	1.2363e-3
<i>Low gross mass</i>	1089.1	9.1817e-4	
<i>Mid gross mass</i>	1014.7	9.8550e-4	

Table 3.13: $\left(\frac{1}{SAR}\right)_{AVG}$ calculation

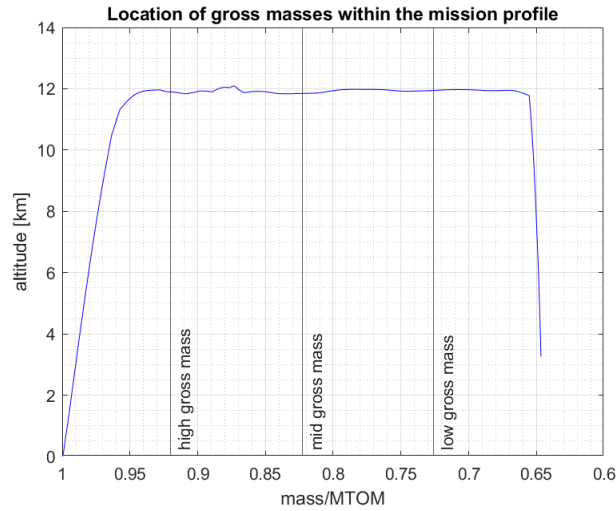


Figure 3.14: Location of gross masses within the mission profile

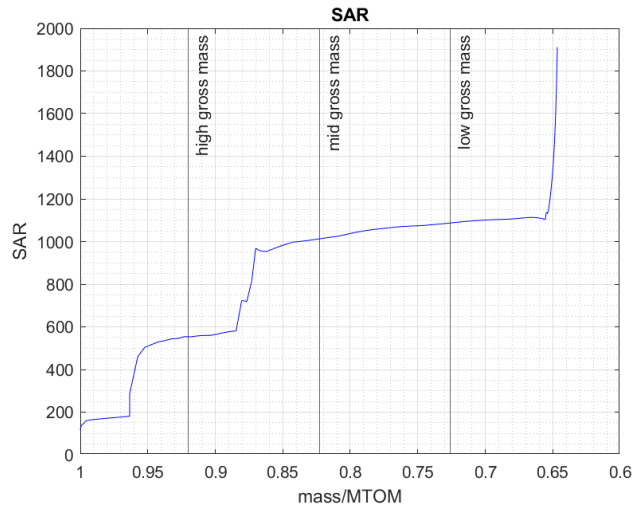


Figure 3.15: SAR – mass/MTOM

3.4.3 RGF calculation

The *Reference Geometric Factor (RGF)* is based on the misuration of the fuselage’s dimension, normalised by dividing for an unitary section.

$$RGF = \frac{area_{floor}}{1 [m^2]}$$

The case of Falcon 10 X falls into categoru *a)*, between the two proposed in the document:

“a) for aeroplanes with a single deck determine the area of a surface (expressed in m2) bounded by the maximum width of the fuselage outer mould line (OML) projected to a flat plane parallel with the main deck floor;” (Annex 16 – Volume III, Appendix 2, ICAO, 2017)

Moreover, in the document could be read:

“2. The RGF includes all pressurised space on the main or upper deck including aisles, assist spaces, passage ways, stairwells and areas that can accept cargo and auxiliary fuel containers. It does not include permanent integrated fuel tanks within the cabin or any unpressurized fairings, nor crew rest/work areas or cargo areas that are not on the main or upper deck (e.g. ‘loft’ or under floor areas). RGF does not include the cockpit crew zone.” (Annex 16 – Volume III, Appendix 2, ICAO, 2017)

What has been just said is presented Figure 3.16, shown in the document *Annex 16 – Volume III, Appendix 2*.

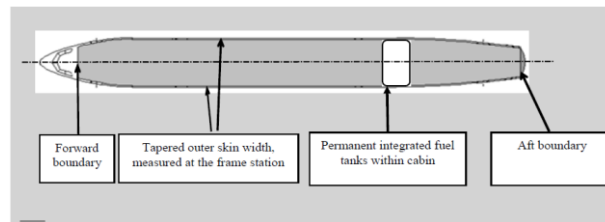


Figure 3.16: RGF

The Falcon 10 X has been modeled with a circular fuselage; therefore, the line identifying the floor must be located below the diameter of the aircraft's section, as described in Figure 3.17, which is also presented in *Annex 16 – Volume III* of the document.

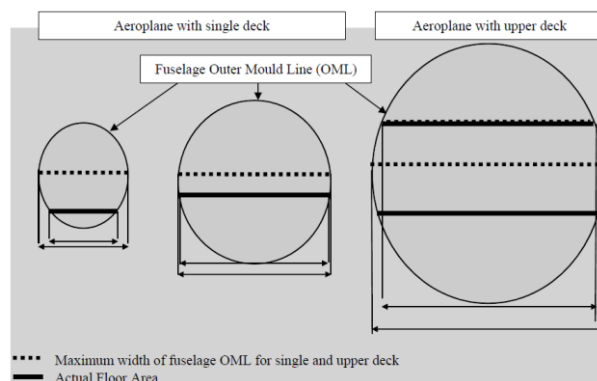


Figure 3.17: Examples of Fuselage Outer Mould Line (OML) and Floor Area; at the centre the case of Falcon 10 X

The RGF was evaluated using the SolidWorks program. The calculation of the floor position was done by subtracting the cabin height from the fuselage diameter:

$$h_{floor} = D_{fuselage} - h_{cabin}$$

The height of the floor is to be considered measured from a point on the circumference to a point inside the section, moving along a diameter. The values considered are presented in Table 3.14.

Fuselage diameter [m]	2.77
Cabin height [m]	2.03
Floor height [m]	0.74

Table 3.14: Calculation of the floor height

With the height of the floor determined, a plane was created in SolidWorks that would cut longitudinally through the aircraft's fuselage, isolating the desired area for evaluation. The sketch of this area is shown in Figure 3.20, and the results are presented in Table 3.15.

$area_{floor} [m^2]$	62.97
<i>RGF</i>	62.97

Table 3.15: RGF results

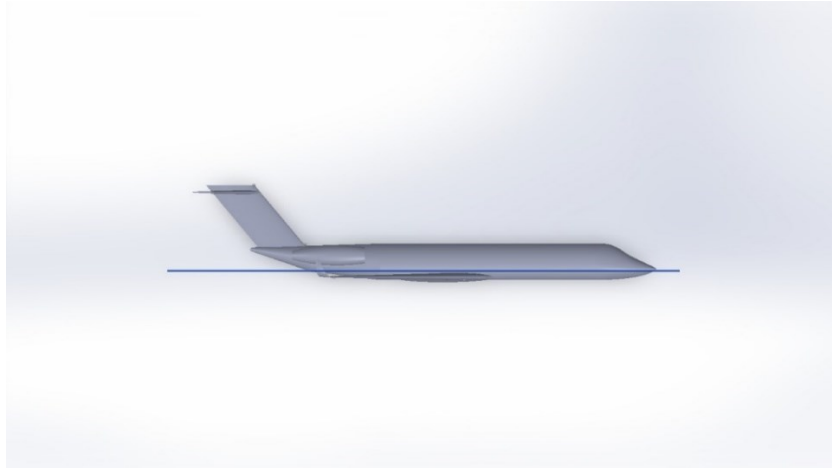


Figure 3.18: Floor plane



Figure 3.19: Section on the floor plane

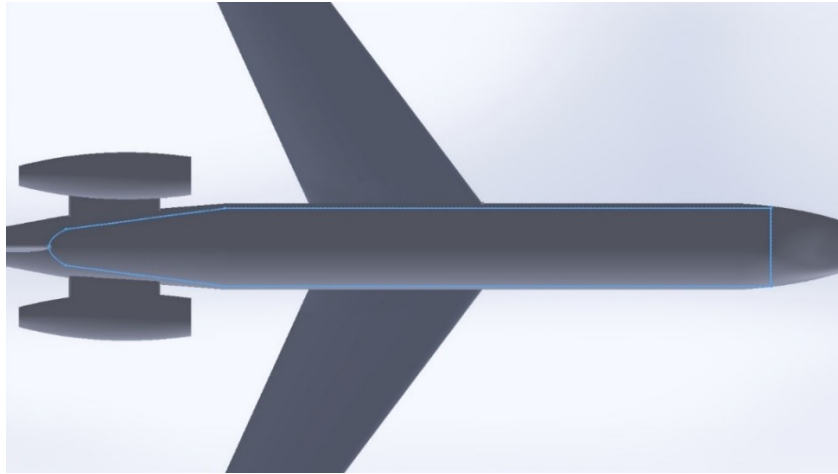


Figure 3.20: Section on the floor plane – zoom

3.4.4 Valuation of CO₂ metric value

The equation presented in Subparagraph 3.4.1 is applied and the result is reported in Table 3.16.

<i>CO₂ metric value [kg/km]</i>	0.4575
<i>Maximum permitted CO₂ metric value [kg/km]</i>	0.7209

Table 3.16: CO₂ metric value

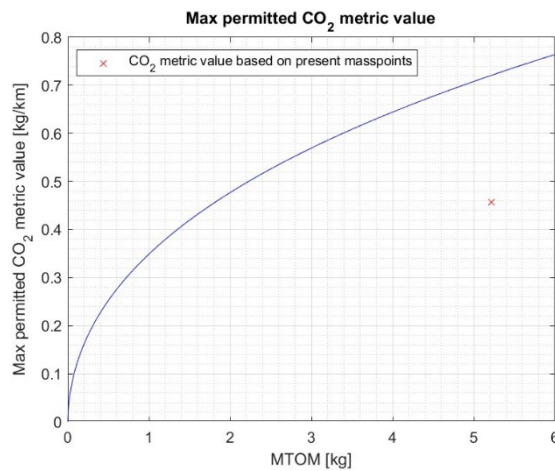


Figure 3.21: Comparison with the maximum permitted metric value of CO₂

Capitolo 4

CO₂ METRIC VALUE ACQUISITION – HIGH-FIDELITY ANALYSIS

In Chapter 4, the steps taken to arrive at the calculation of the CO₂ metric value are discussed in detail in order to realize a *high fidelity analysis* that starts from an aerodynamic simulation, based on a CFD analysis, and ends with the calculation proposed in *Annex 16 – Volume 3, “CO₂ Certification Requirements”*. Since the propulsive database used is the same for both low-fidelity and high-fidelity analysis, it will not be discussed in this chapter.

4.1 Aerodynamics simulation

4.1.1 Mesh

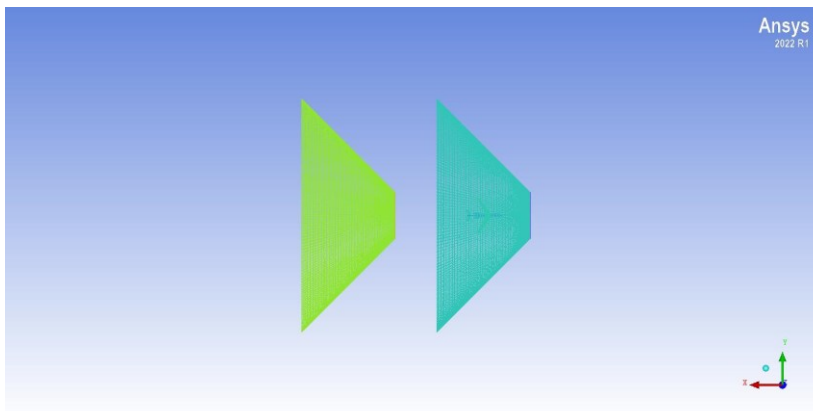
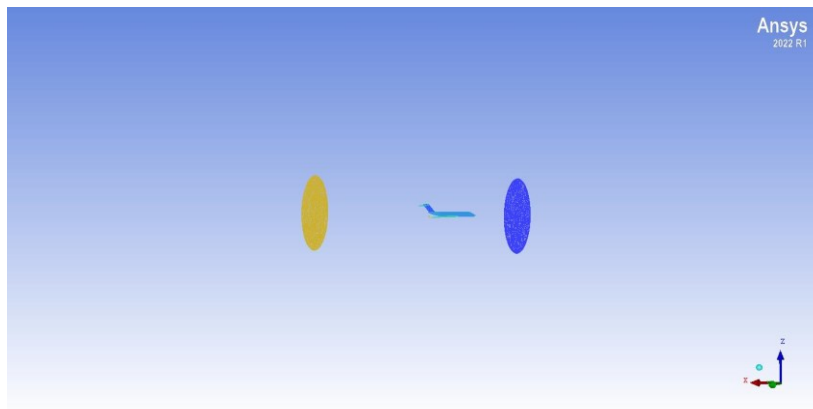
The calculation domain was realised taking the body length L of the aircraft, as the reference measurement; the shape of the domain consists of a truncated cone extending from one body length in relation to the nose to one body length in relation to the tail. Another truncated cone, identical to the first, is located two body lengths away from the tail; the two truncated cones are connected by a cylinder. Each of these geometric elements was assigned a function and the associations are presented in Table 4.1. The extremes of the domain, consisting of inlet and outlet, are positioned at the chosen distance as not to generate numerical dirt, so the inlet has been positioned one body length away from the nose and the outlet two body lengths away from the tail.

<i>Part name</i>	<i>Location</i>	<i>Dimensions [m]</i>
<i>Inlet</i>	1L from the nose	$r \approx \frac{1}{2}b \approx 19.32$
<i>Inlet far field</i>	Minor base: 1L from the nose Major base: 1L from the tail	$r_{min} = r \approx 19.32$ $r_{max} = 4r \approx 77.28$ $h = 3L = 100.2$
<i>Inlet external layer</i>	First base: 1L from the tail	$r = 4r \approx 77.28$

	Second base: $4L$ from the tail	
<i>Outlet</i>	$2L$ from the tail	$r \approx \frac{1}{2}b \approx 19.32$
<i>Outlet far field</i>	Minor base: $2L$ from the tail Major base: $5L$ from the tail	$r_{min} = r \approx 19.32$ $r_{max} = 4r \approx 77.28$ $h = 3L = 100.2$

Table 4.1: Computational domain dimensions

The table considered the aircraft body length L and wing span b , which are 33.4 m and 38.64 m respectively.



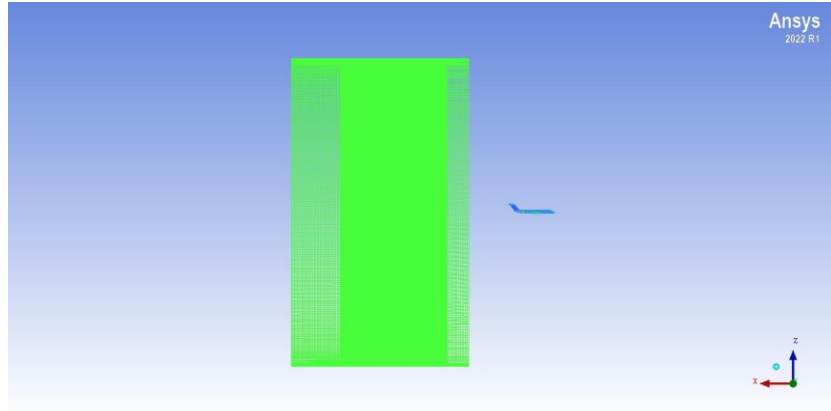
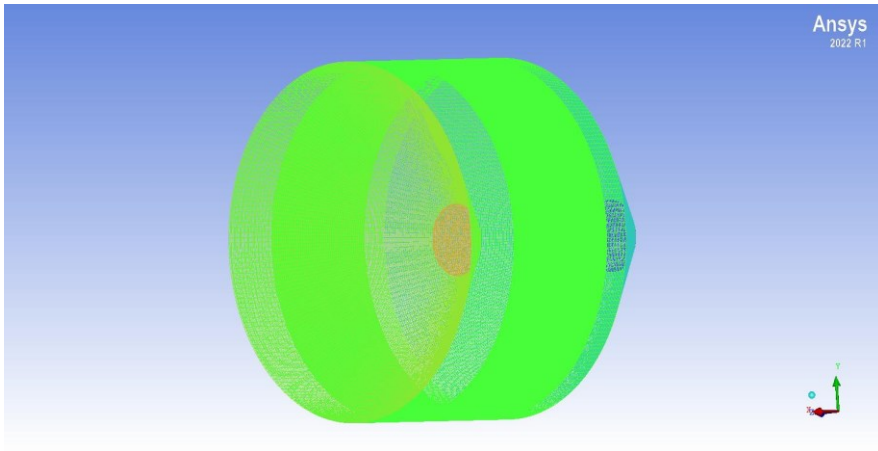
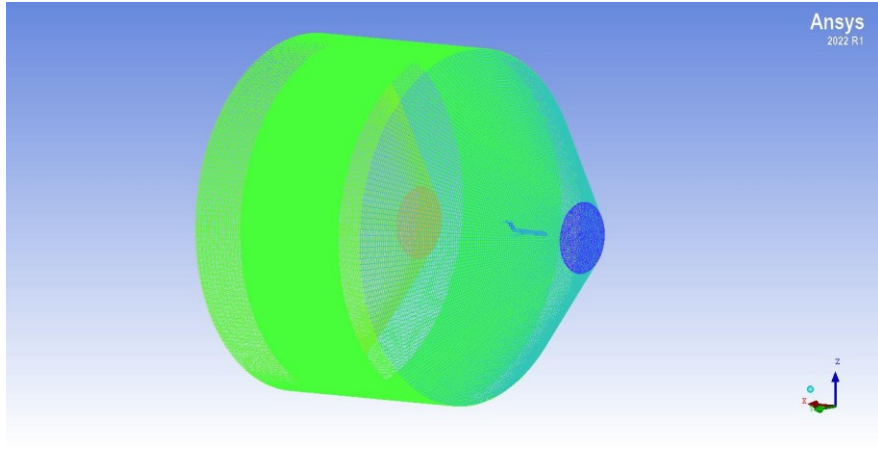


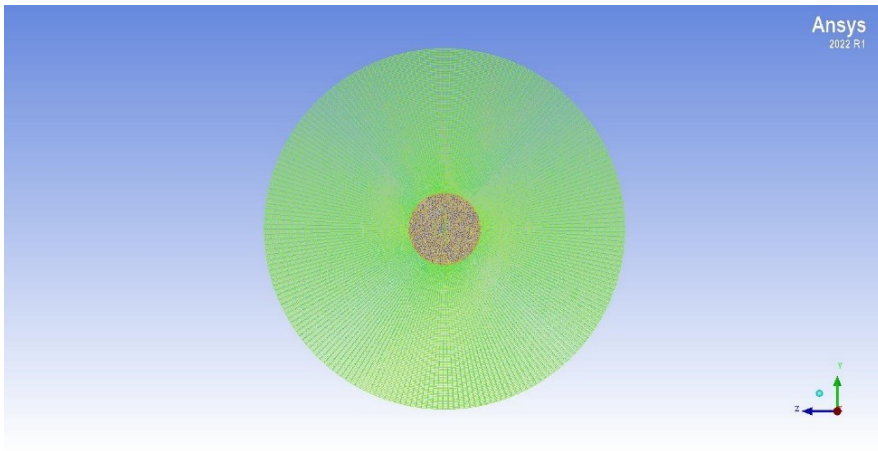
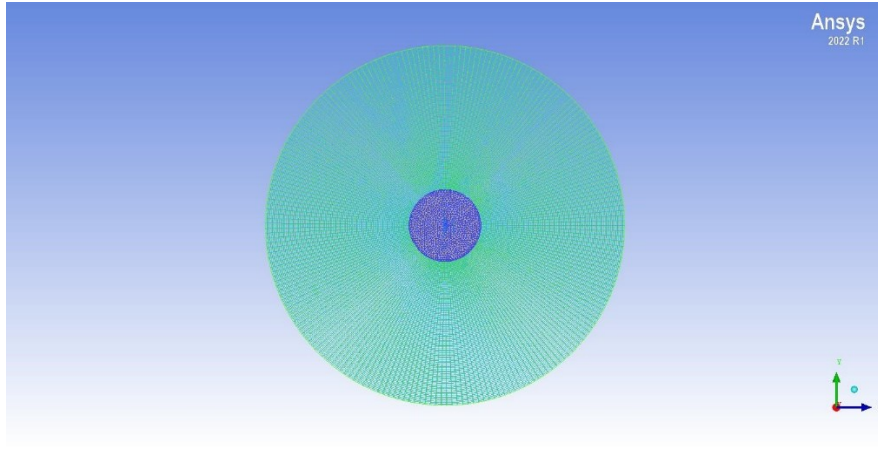
Figure 4.1: Parts of the computational domain: 1 inlet and outlet, 2 inlet and outlet far field, 3 inlet external layer

The grid was subdivided into two blocks, an unstructured external one and a structured internal one. The structured grid is limited to a block encompassing the aircraft because extending it to the entire domain was complex for an irregular geometry such as the one of the case study; at the same time, the structured grid was chosen after testing with an entirely unstructured grid that gave unlikely results, so, to avoid problems of numerical dispersion, the choice fell to a structured grid. Another advantage of this type of grid is that it saves on the number of elements to complete the grid. The exact number of elements of the mesh and their shape are presented in Table 4.2 while the total number of elements is 9973894.

<i>Element type</i>	<i>Number of elements</i>
<i>Tetrahedral</i>	4032062
<i>Hexahedral</i>	5526144
<i>Triangular</i>	264488
<i>Quadrangular</i>	98064
<i>Pyramidal</i>	53136

Table 4.2: Elements' shape and number





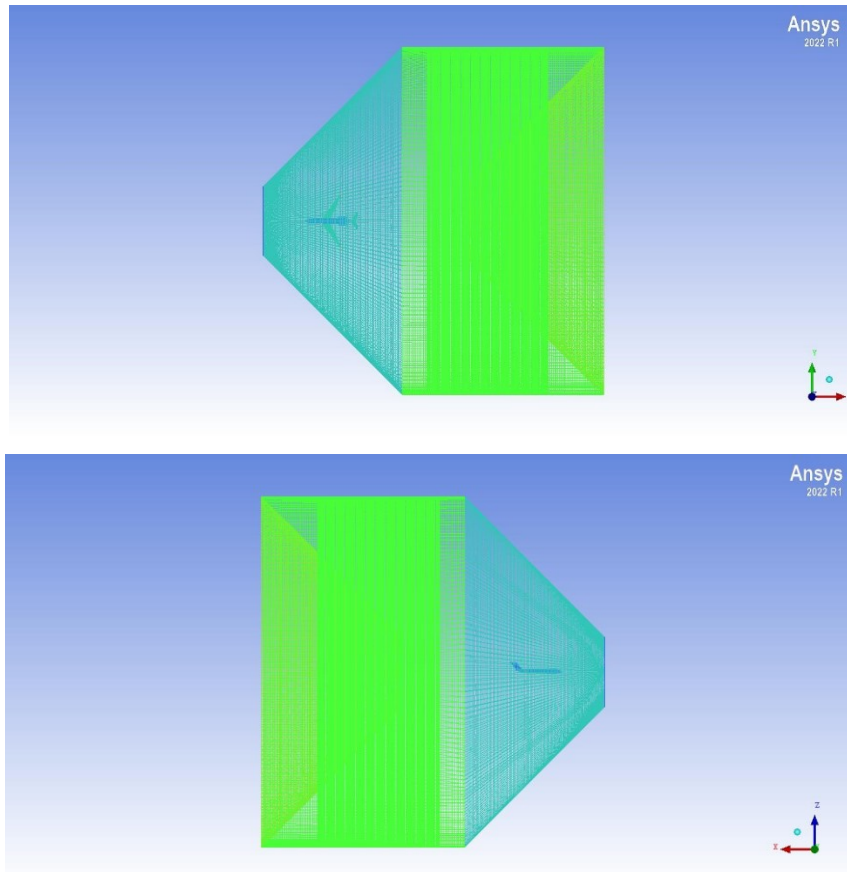


Figure 4.2: Mesh views: 1-2 diagonal, 3 front, 4 retro, 5-6 lateral

4.1.2 Solver description – Ansys Fluent

CFD simulations are conducted utilizing both the commercial Ansys Fluent 2022 R1 code. Ansys Fluent is one of the most sophisticated software packages for computational fluid dynamics simulation, widely used both in academia and in industrial sectors such as aerospace, automotive, power engineering and many others. Thanks to its versatility and accuracy, Fluent enables in-depth analysis of the behaviour of fluids in motion, whether air, water, gases or complex liquids.

One of the features that makes Ansys Fluent particularly powerful is its ability to handle complex simulations through advanced turbulence models. This is essential for applications where the disordered and swirling motion of fluid plays a key role, such as in optimising the shape of vehicles to improve aerodynamics. Fluent also allows the simulation of multiphase flows, so the software is capable of analysing how different phases behave, for example in the case of a fluid that contains both gases and solid particles, or phenomena such as cavitation and mixing of liquids.

Fluent's attention to detail is also evident in its ability to simulate heat transfer, a crucial element in many industries. This allows engineers and designers to calculate and visualise how heat moves through materials by conduction, convection or radiation, a valuable tool for designing cooling systems in electronic devices, improving engine efficiency, or developing new heat transfer technologies.

4.1.3 *Eulero equations*

An inviscid flow of a compressible gas in a parallel pipe, follows the conservation laws for mass, momentum and energy:

$$\begin{aligned}\rho_t + (\rho u)_x &= 0 \\ (\rho u)_t + (p + \rho u^2)_x &= 0 \\ (\rho e)_t + (\rho u e + up)_x &= 0\end{aligned}$$

Where t is time, x distance, ρ the density, u the velocity, p the pressure and e the specific total energy. To close the system, an equation of state has to be added:

$$p = p(\rho, i)$$

By calling γ the ratio of specific heats of an ideal gas, the equation of state can be written as follows:

$$p = (\gamma - 1)\rho i$$

Where i is the specific internal energy:

$$i = e - \frac{1}{2}u^2$$

The three conservation laws can be compacted in the form

$$\bar{w}_t + \bar{F}_x = 0$$

Where \bar{w}_t is the vector of conservative variables derived in time, and \bar{F}_x is the vector of flows of conservative variables derived in space:

$$\bar{w} = \begin{bmatrix} \rho \\ \rho u \\ \rho e \end{bmatrix}$$

$$\bar{F} = \begin{bmatrix} \rho u \\ p + \rho u^2 \\ \rho u e + up \end{bmatrix}$$

Applying the Gauss' divergence theorem to the equations written in this form, we have:

$$\oint \bar{w} dx - \bar{F} dt = 0$$

Around any closed contour in (x, t) .

From these equations, we can obtain the system of characteristic equations

$$\begin{aligned}
dp - \rho a du &= 0 \quad \text{along } dx = (u - a)dt \\
dp - a^2 d\rho &= 0 \quad \text{along } dx = u dt \\
dp + \rho a du &= 0 \quad \text{along } dx = (u + a)dt
\end{aligned}$$

We introduce the sound speed a

$$a^2 = \frac{\partial p}{\partial \rho}$$

Since we have an isentropic process, we know how pressure and density bind

$$d\left(\frac{p}{\rho^\gamma}\right) = 0$$

So we have

$$a = \sqrt{\gamma RT}$$

The Euler equations can now be discretized by dividing the computational domain into a series of equispaced cells of Δx . One can write the balance equation for the N -th cell, centred in x_N

$$\frac{\partial}{\partial t} \int_{x_{N-1/2}}^{x_{N+1/2}} \bar{w}(x, t) dx - \bar{F}\left(x_{N+1/2}, t\right) + \bar{F}\left(x_{N-1/2}, t\right) = 0$$

The integral of the conservative quantities can be replaced with its mean value in the cell centred in x_N

$$\int_{x_{N-1/2}}^{x_{N+1/2}} \bar{w}(x, t) dx = \bar{w}_m \Delta x$$

If, however, we approximate \bar{w}_m with \bar{w}_N , the conservative value at the cell centre, the balance equation then becomes

$$\frac{\partial \bar{w}_N}{\partial t} \Delta x - \bar{F}\left(x_{N+1/2}, t\right) + \bar{F}\left(x_{N-1/2}, t\right) = 0$$

Since the vector of convective flows is a function of conservative quantities, we can write

$$\frac{\partial \bar{w}_N}{\partial t} \Delta x - \bar{F}\left[\bar{w}\left(x_{N+1/2}, t\right)\right] + \bar{F}\left[\bar{w}\left(x_{N-1/2}, t\right)\right] = 0$$

The vector of conservative quantities appears at the cell centre but also at the interfaces of the cell.

Integrating in time between instants t_k, t_{k+1} , we have

$$[\bar{w}_N(x, t_{k+1}) - \bar{w}_N(x, t_{k-1})] \Delta x - \int_{t_k}^{t_{k+1}} \bar{F}\left[\bar{w}\left(x_{N+1/2}, t\right)\right] dt + \int_{t_k}^{t_{k+1}} \bar{F}\left[\bar{w}\left(x_{N-1/2}, t\right)\right] dt = 0$$

Considering that the time-averaged value of the fluxes of conservative quantities can be written as

$$f_{N+1/2}^k = \frac{1}{\Delta t} \int_{t_k}^{t_{k+1}} \bar{F} \left[\bar{w} \left(x_{N+1/2}, t \right) \right] dt$$

You get

$$w_N^{k+1} = w_N^k - \frac{\Delta t}{\Delta x} \left(f_{N+1/2}^k - f_{N-1/2}^k \right)$$

One can make an approximation and say that the flow function $f(w(x, t))$ all'interfaccia tra two cells can be expressed as a function of the values of the conservative quantities in the cell centres of the cells divided by the interfaces $N + \frac{1}{2}$ and $N - \frac{1}{2}$. Thus we have

$$w_N^{k+1} = w_N^k - \frac{\Delta t}{\Delta x} \left(F(w_N^k, w_{N+1}^k) - F(w_N^k, w_{N-1}^k) \right)$$

An equation was obtained that can be implemented numerically, given the function F with which the flows at the interfaces are to be modelled.

4.1.4 Riemann problem

The Euler equations constitute a hyperbolic system of equations, thus having all real eigenvalues. Solving such a system yields solutions with discontinuities, and the Riemann problem provides a theoretical resolution of such discontinuities. A hyperbolic system of partial differential equations (PDE) is a type of mathematical system that describes the time evolution of physical phenomena characterised by waves and propagation of signals with finite velocities. These systems are fundamental in modelling many natural phenomena, such as the behaviour of compressible fluids, the propagation of acoustic and electromagnetic waves, and elastic waves in solids. Moreover, Hyperbolic systems are characterised by different types of waves, such as compression waves, which are discontinuities in the system's solution for which there is an increase in pressure, expansion waves, for which there is a decrease in pressure, and contact surfaces, which constitute a discontinuity in the density field but not in the pressure field.

Euler equations can be written in the form

$$\bar{U}_t + \tilde{A} \bar{U}_x = 0$$

Using a set of variables such as speed of sound a , flow velocity u and entropy S , one can diagonalise the coefficient matrix \tilde{A} so as to obtain a system of the type

$$\bar{R}_t + \Lambda \bar{R}_x = 0$$

Where Λ is a matrix that has on its main diagonal the eigenvalues of the system:

$$\lambda_1 = u - a$$

$$\lambda_2 = u$$

$$\lambda_3 = u + a$$

The eigenvalues of the system represent three waves propagating with speed $u - a$, u , $u + a$ in the motion field. From the eigenvalues, the eigenvectors of the system can be found, thanks to which the original system of PDEs can be rewritten as a system of decoupled ODEs, which allows the Riemann invariants to be found:

$$\begin{cases} dR_1 \\ dR_2 \\ dR_3 \end{cases} = \begin{cases} \frac{2}{\gamma - 1} da - du - \frac{a}{\gamma(\gamma - 1)} dS \\ dS \\ \frac{2}{\gamma - 1} da + du - \frac{a}{\gamma(\gamma - 1)} dS \end{cases}$$

By integrating the Riemann invariants along the respective λ , you always get 0. To understand the meaning of this, one can represent in a plane $t - x$ the signals R_1 , R_2 and R_3 , each having as a slope its own propagation speed λ_1 , λ_2 and λ_3 .

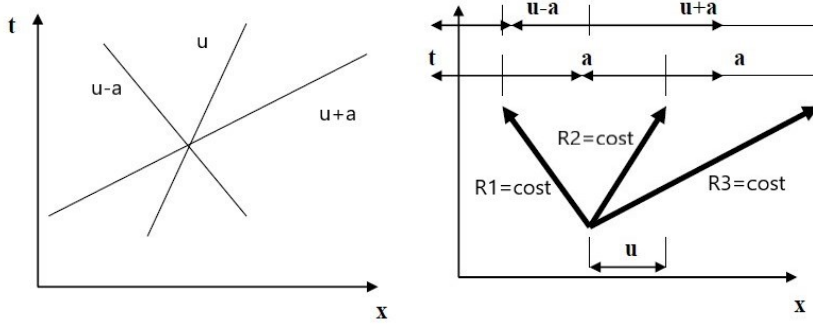


Figure 4.3: Signals for a subsonic case of study

The integral of the Riemann invariant along the relevant characteristic line is zero, so the R signals remain constant along their characteristic lines λ .

Solving the Riemann problem means following the time evolution of a discontinuity present at the initial time and this can be done by various methods, such as the upwind method, Godunov's methods, or, as in the present case, the Roe method.

4.1.5 Approximate Riemann solvers – Roe's method (1981)

Roe proposed a method exploiting the fact that the Riemann solution for any set of linear conservation laws is easily computed. The key idea is to linearise the non-linear Euler equations, transforming them into a linear system that can be solved in a similar way to a simple Riemann problem. This linearisation is achieved using the Roe matrix, which is an approximate Jacobian matrix of flows.

The equation

$$\bar{w}_t + \bar{F}_x = 0$$

With \bar{F} a linear function of \bar{w} , can be written as

$$\bar{w}_t + A\bar{w}_x = 0$$

Where A is a constant Jacobian matrix where the derivatives of \bar{F} with respect to \bar{w} appear.

Given two states \bar{w}_L, \bar{w}_R , the flux difference can be uniquely written as

$$\bar{F}_R - \bar{F}_L = \sum \alpha_k \lambda_k \bar{e}_k$$

Where \bar{e}_k are the right eigenvectors of A , α_k is the strength of the k-th wave and λ_k (an eigenvalue of A) is its velocity. The flux at the interface could be expressed as

$$\bar{F}_{i+\frac{1}{2}}(\bar{w}_L, \bar{w}_R) = \bar{F}_L + \sum \alpha_k \lambda_k \bar{e}_k^{(-)} \quad \text{or} \quad \bar{F}_{i+\frac{1}{2}}(\bar{w}_L, \bar{w}_R) = \bar{F}_R - \sum \alpha_k \lambda_k \bar{e}_k^{(+)}$$

Where superscripts ‘-’ and ‘+’ represent the summation over the negative and positive speeds. Mediating the two expressions we have

$$\bar{F}_{i+\frac{1}{2}}(\bar{w}_L, \bar{w}_R) = \frac{1}{2}(\bar{F}_L + \bar{F}_R) - \frac{1}{2} \sum \alpha_k |\lambda_k| \bar{e}_k$$

To linearise the problem, an $\tilde{A}(\bar{w}_L, \bar{w}_R)$ -matrix must be found whose eigenvalues and eigenvectors satisfy the following two equations

$$\bar{F}_R - \bar{F}_L = \sum \alpha_k \lambda_k \bar{e}_k$$

$$\bar{w}_L - \bar{w}_R = \sum \alpha_k \bar{e}_k$$

The method returns exact values whenever \bar{w}_L, \bar{w}_R are on opposite sides of a shock wave or contact discontinuity. When this happens, the Rankine-Hugoniot relationship must apply

$$\bar{F}_R - \bar{F}_L = S(\bar{w}_L - \bar{w}_R)$$

Where S is the shock speed. Se queste ultime tre equazioni sono verificate, si ha

$$S\alpha_k = \lambda_k \alpha_k, \quad \forall k$$

Roe gave expressions for $\alpha_k, \tilde{\lambda}_k$ and \tilde{e}_k

$$\tilde{e}_1 = \begin{bmatrix} 1 \\ \tilde{u} - \tilde{a} \\ \tilde{h} - \tilde{u}\tilde{a} \end{bmatrix}, \quad \tilde{e}_2 = \begin{bmatrix} 1 \\ \tilde{u} \\ \frac{1}{2}\tilde{u}^2 \end{bmatrix}, \quad \tilde{e}_3 = \begin{bmatrix} 1 \\ \tilde{u} + \tilde{a} \\ \tilde{h} + \tilde{u}\tilde{a} \end{bmatrix}$$

$$\tilde{\lambda}_1 = \tilde{u} - \tilde{a}, \quad \tilde{\lambda}_2 = \tilde{u}, \quad \tilde{\lambda}_3 = \tilde{u} + \tilde{a}$$

$$\alpha_1 = \frac{1}{2\tilde{a}^2} [\Delta p - \tilde{\rho}\tilde{a}\Delta u], \quad \alpha_2 = \frac{1}{2\tilde{a}^2} [\tilde{a}^2\Delta\rho - \Delta p], \quad \alpha_3 = \frac{1}{2\tilde{a}^2} [\Delta p + \tilde{\rho}\tilde{a}\Delta u]$$

Where

$$\tilde{\rho}^2 = \rho_L \rho_R$$

$$\tilde{u} = \frac{\rho_L^{\frac{1}{2}} u_L + \rho_R^{\frac{1}{2}} u_R}{\rho_L^{\frac{1}{2}} + \rho_R^{\frac{1}{2}}}$$

$$\tilde{h} = \frac{\frac{1}{\rho_L^2} h_L + \frac{1}{\rho_R^2} h_R}{\frac{1}{\rho_L^2} + \frac{1}{\rho_R^2}}$$

$$\tilde{a}^2 = (\gamma - 1) \left[\tilde{h} - \frac{1}{2} \tilde{u}^2 \right]$$

The Jacobian matrix \tilde{A} is

$$\tilde{A} = \begin{bmatrix} 0 & 1 & 0 \\ \frac{\gamma - 3}{2} \tilde{u}^2 & (3 - \gamma) \tilde{u} & \gamma - 1 \\ \tilde{u} \left(\frac{\gamma - 1}{2} \tilde{u}^2 - \tilde{h} \right) & \tilde{h} - (\gamma - 1) \tilde{u}^2 & \gamma \tilde{u} \end{bmatrix}$$

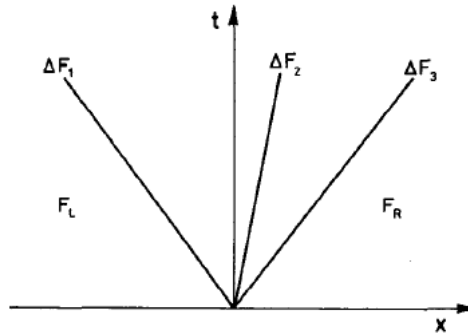


Figure 4.4: Diagram for computing interface flux

4.1.6 Simulation setting

I primi step sono impostare la corretta unità di misura, andando a usare i millimetri come scala e scegliere un modello *density based*, quindi compressibile. Successivamente viene attivata l'equazione dell'energia, dopodichè si sceglie di risolvere il modello inviscido di Eulero, questo passaggio quindi suggerisce che nella simulazione non verranno considerati effetti di strato limite, né di turbolenza.

At this point we move on to the choice of materials. For the fluid environment, the *air* mixture is chosen, and it is required to be treated as an ideal gas, so it will have constant specific heats, the internal energy will depend only on temperature, and the equation of state of perfect gases will apply. The material chosen for the fuselage, however, is *aluminium*.

The boundary condition chosen for the *inlet*, *inlet far field* and *inlet external layer* is that of *pressure far field*, which allows the simulation of an ideally compressible flow that is far away from the body and moving at a constant velocity. In this field you can enter the Mach number you wish to simulate and specify the direction of the fluid current, in the form of the

cosine and sine of the desired angle of attack. The temperature and pressure at the chosen altitude, presented in Table 4.4, must also be specified here.

The boundary condition for the inner parts of the domain is *interior*, which allows the configuration of an inner surface through which the flow can flow freely. On all aircraft components, such as nacelles, fuselage, tail, wing, etc., the *wall* condition is set, which instead allows all those surfaces through which the flow does not pass.

The boundary condition chosen for the *outlet*, *outlet far field* is that of *pressure far field*, is *pressure outlet*, which allows you to set the static flow pressure, which would be that of the external current. The temperature and pressure at the chosen altitude, presented in Table 4.4, must also be specified here.

The analysis was carried out for different Mach numbers M and, for each Mach, for different angles of attack α . The various combinations are presented in Table 4.3.

M	α [deg]
0.3	0
	5
	10
0.6	0
	5
	10
0.8	0
	5
	10
0.9	0
	5
	10

Table 4.3: Mach numbers and angles of attack

The simulations were set considering an altitude of 12000 m, for which we have the atmospheric conditions presented in Table 4.4.

Altitude [m]	12000.0
Pressure [Pa]	19333.6
Temperature [K]	216.6
Density [kg/m³]	0.3108
Sound speed [m/s]	295.1

Table 4.4: Atmosphere conditions at 12000 m

The reference quantities considered are the wing area and the mean aerodynamic chord, the values of which are presented in Table 4.5.

<i>Wing surface [m²]</i>	120
<i>Mean aerodynamic chord [m]</i>	4.60

Table 4.5: Reference values

The chosen numerical method is formulated implicitly and the Rieman problem is solved by applying the finite-difference ROE method; the pressure gradient is calculated using the Green-Gauss method and a simulation is first set to the first order of accuracy, then, after 15,000 iterations, a new simulation is re-set to the second order of accuracy.

In the output we want to obtain the values of C_x , C_z and C_{m_y} , then the monitors must be constructed, choosing the *force coefficient* option for the first two and the *moment coefficient* one for the last.

4.1.7 Test matrix

The output of the simulation were the components C_x , C_z and C_{m_y} , then the following formulas were applied to derive the lift and drag coefficients:

$$C_L = C_z \cdot \cos(\alpha) - C_x \cdot \sin(\alpha)$$

$$C_D = C_x \cdot \cos(\alpha) + C_z \cdot \sin(\alpha)$$

Where C_x is the force coefficient in the x-direction, C_z is the force coefficient in the z-direction and C_{m_y} is the coefficiente di momento. α is the angle of attack, expressed in radians.

The results at the first order of accuracy are presented in Table 4.6, with corresponding graphs, where the quantities are presented as a function of angle of attack in degrees.

Initial conditions		I order			II order		
<i>M</i>	<i>α [deg]</i>	C_L	C_D	C_{m_y}	C_L	C_D	C_{m_y}
0.3	0	0.20789	0.052459	-0.82859	0.25975	0.02922	-1.05400
	5	0.73838	0.083966	-3.1000	0.79357	0.05629	-3.32440
	10	1.1525	0.17447	-4.8560	1.12609	0.12336	-4.68180
0.6	0	0.23237	0.055082	-0.94312	0.29584	0.03058	-1.21690
	5	0.80575	0.097572	-3.3942	0.87325	0.06302	-3.65940
	10	1.2124	0.19344	-5.1031	1.13488	0.15409	-4.70940
0.8	0	0.26103	0.059430	-1.0740	0.36578	0.03597	-1.52480

	5	0.95200	0.11544	-4.0409	1.12739	0.09871	-4.75630
	10	1.4663	0.26348	-6.1980	1.88880	0.25500	-7.98780
0.9	0	0.30558	0.079348	-1.3162	0.42819	0.05289	-1.89090
	5	1.02058	0.170938	-4.6513	1.09212	0.15937	-5.27200
	10	1.55801	0.338909	-6.8687	1.75620	0.43290	-8.65290

Table 4.6: Test matrix, I and II order accuracy

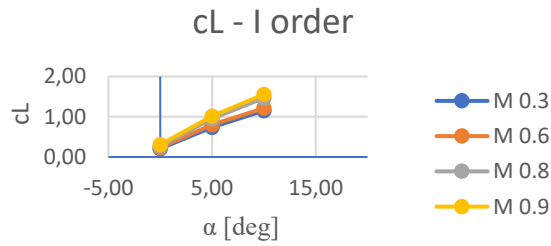


Figure 4.5: Lift coefficient – I order

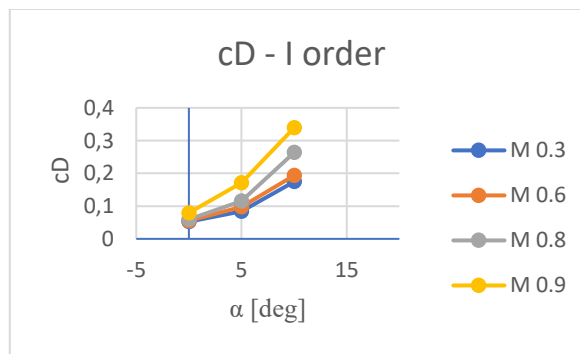


Figure 4.6: Drag coefficient – I order

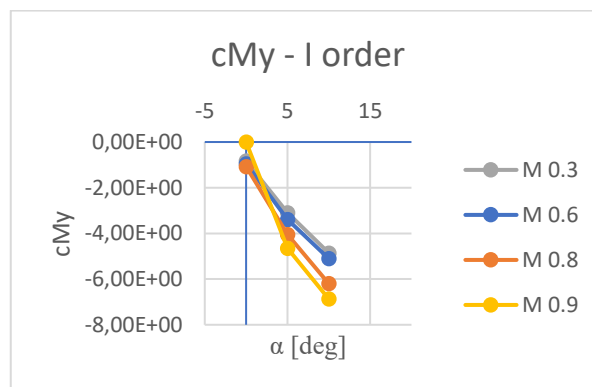


Figure 4.7: Moment coefficient – I order

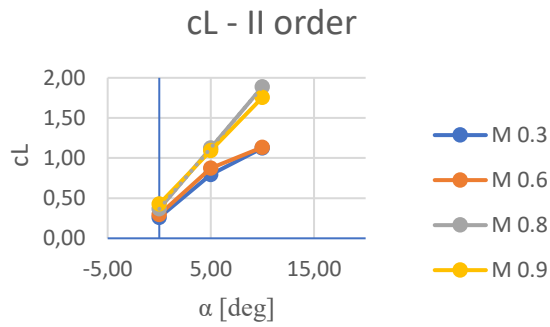


Figure 4.8: Lift coefficient - II order

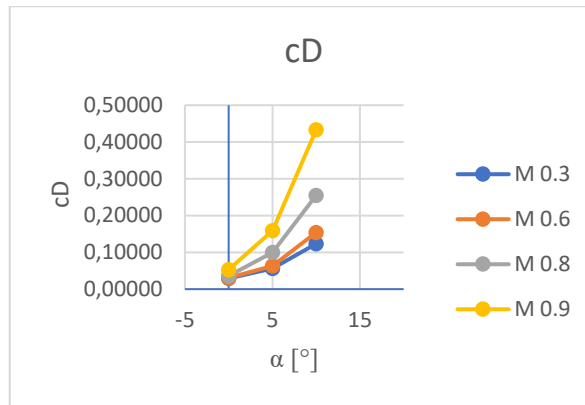


Figure 4.9: Drag coefficient - II order

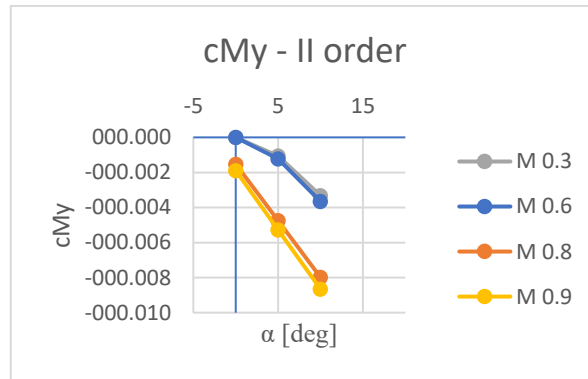


Figure 4.10: Moment coefficient - II order

4.2 Mission simulation

As anticipated, the characteristics of the propulsion system are defined only once, so the database entered in ASTOS remains that of the low-fidelity analysis; the aerodynamic database, on the other hand, is replaced by the results of the CFD analysis.

During the *Climb phase* a linear control law was maintained, using the *Euler Angles*, in particular the pitch angle, as the control variable; the range of angles considered goes from

4.00 to 6.00 degrees. The throttle was first set on 1. The phase duration is 30 minutes, but the final altitude is reached after 50 minutes.

The Cruise phase is the longest one, since it lasts about 16 hours at a constant altitude of 15500 m and a Mach number growing from 0.70 to 0.82. In this case the simulation was made by changing the *Aerodynamics Angles*, in particular the angle of attack, which was set on 4.30° at the beginning of the phase and gradually decreased to 2.80° . The throttle was initially set on 0.8, then lowered to 0.65.

The final phase, the *Approach* one, lasts 50 minutes and was still made by modifying the Euler angles, in particular the pitch one.

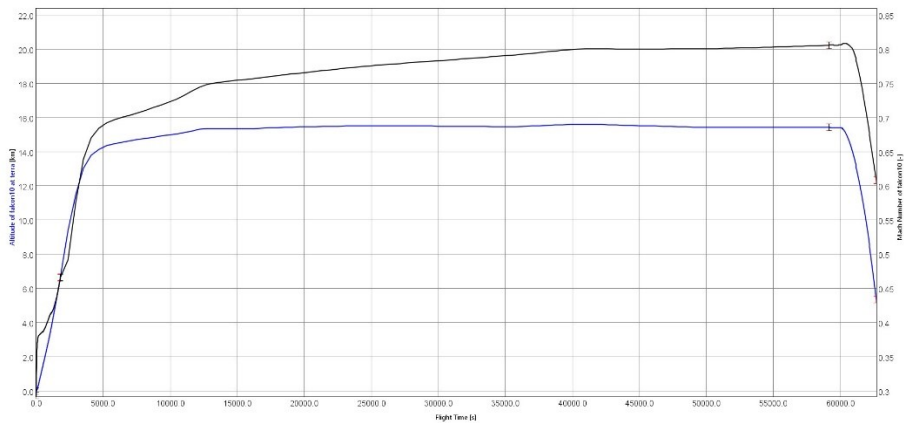


Figure 4.11: Altitude, Mach number vs time

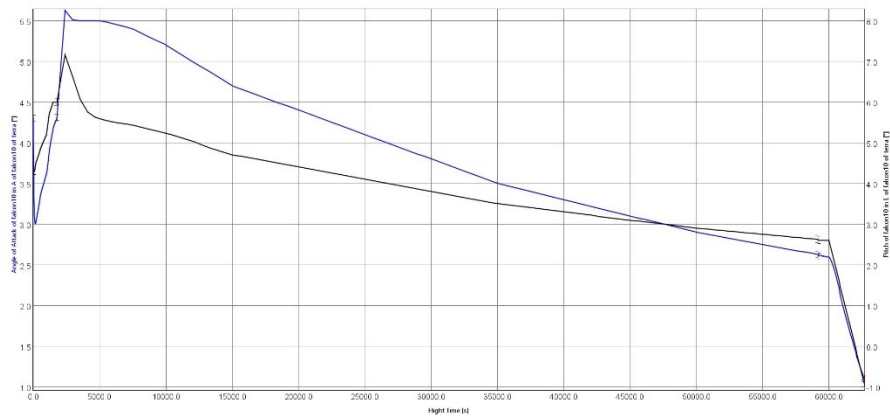


Figure 4.12: Angle of attack, Pitch angle vs time

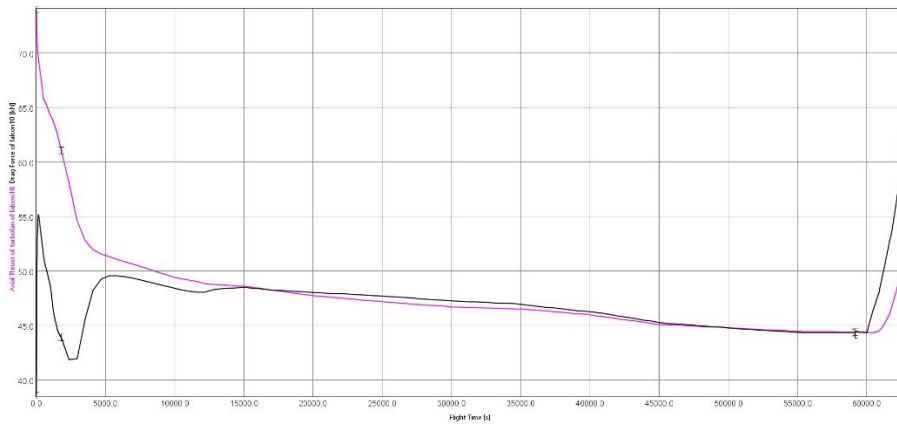


Figure 4.13: Thrust, Drag force vs time

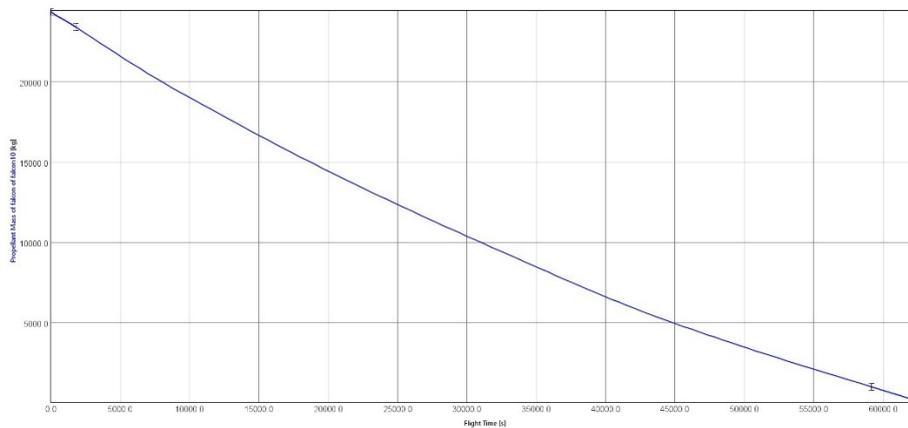


Figure 4.14: Propellant mass vs time

4.3 Application of the standard

Since the aircraft remains the same in the two analyses, the MTOM does not vary and, consequently, the high, mid and low gross masses do not change either. The new values found for aerodynamics, on the other hand, vary the mass flow during the mission and, therefore, also the fuel consumption.

The same parameters presented in Table 3.12 are imported from ASTOS, which this time take on obviously different values, as can be seen in Table 4.7.

	T [K]	a [m/s]	M	TAS [m/s]	W_f [kg/s]	SAR [km/kg]
<i>High gross mass</i>	216.65	295.04	0.7066	208.47	0.5149	404.91
<i>Low gross mass</i>	216.65	295.04	0.7845	231.45	0.4383	603.18
<i>Mid gross mass</i>	216.65	295.04	0.7624	224.95	0.3837	513.25

Table 4.7: SAR calculation: temperature, sound speed, Mach number, TAS, fuel mass flow, SAR

At this point, the new SARs can be calculated, inverted and averaged at the three points identified by the gross masses. The results can be seen in Table 4.8.

	<i>SAR [km/kg]</i>	<i>1/SAR [km/kg]</i>	$\left(\frac{1}{SAR}\right)_{AVG}$ [km/kg]
<i>High gross mass</i>	404.91	2.4697e-3	2.0253e-3
<i>Low gross mass</i>	603.18	1.6579e-3	
<i>Mid gross mass</i>	513.25	1.9484e-3	

Table 4.8: $\left(\frac{1}{SAR}\right)_{AVG}$ calculation

The last step is to calculate the metric value of CO₂ and compare it with the maximum value, which remains the same as calculated for the low-fidelity analysis and is shown in Table 3.9. Remember that since the same aircraft is considered, the RGF value calculated in Chapter 3 and presented in Table 3.15 remains the same in the high-fidelity analysis as well. The metric CO₂ value obtained is entered, and compared with the maximum permitted limit, in Table 4.9.

<i>CO₂ metric value [kg/km]</i>	0.7494
<i>Maximum permitted CO₂ metric value [kg/km]</i>	0.7209

Table 4.9: CO₂ metric value

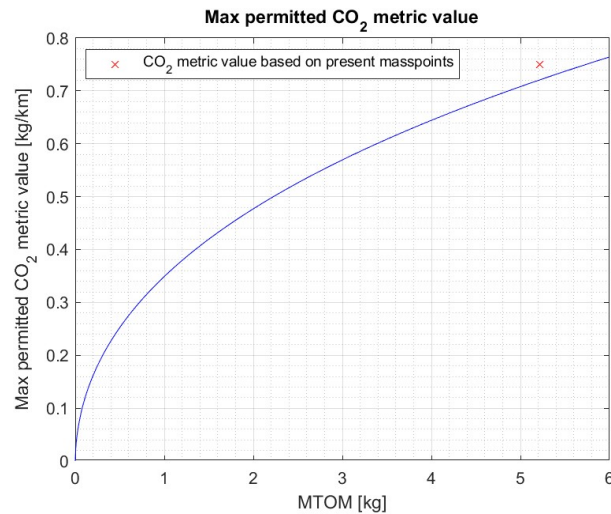


Figure 4.15: Comparison with the maximum permitted metric value of CO₂

Capitolo 5

DISCUSSION OF RESULTS

This chapter will discuss the results obtained from the *low-fidelity analysis* (Chapter 3) and the *high-fidelity analysis* (Chapter 4).

5.1 Discussion of the aerodynamics simulation's results

Raymer's model provides sufficiently accurate estimates for traditional aircraft configurations, such as straight-wing aircraft, derived from semi-empirical relationships based on historical data and induced lift models. These formulae remain valid up to transonic regimes, i.e. up to Mach numbers around 0.90, but may be inaccurate even around the critical zone, i.e. already for Mach numbers of 0.80, since compression beams may develop, which are not captured by the model and which affect the pressure distribution and thus C_L and C_D .

5.1.1 Comparison of Raymer model and CFD results – Lift coefficient

The lift estimates, can be considered accurate in the low subsonic regime, therefore around Mach numbers between 0.3 and 0.6, while in the high subsonic regime, for the reasons just described, the lift could be overestimated because the compressibility effects occurring at such flow velocities are not taken into account.

With regard to the Eulerian analysis conducted with Fluent, it is expected that pressure gradients, as well as the effects of compressibility, will be modelled with greater accuracy up to transonic regimes. It must be emphasised, however, that using this model, viscosity is not introduced into the resolution of the continuity equations, so the lift coefficient may be overestimated: the flow may undergo boundary layer separations that would decrease the lift.

Having said this, it is expected that at Mach numbers 0.30 and 0.60, the lift coefficient calculated by Raymer's model is adequately estimated and this estimation is carried out much more accurately by the CFD analysis; this conclusion can be drawn by observing the Graphs in Figure 5.1, where it can be seen that Raymer's model, since it neglects the three-dimensional effects on the lift distribution, overestimates the C_L especially at high incidences ($\alpha=10^\circ$).

Although at such incidence the correction made by the CFD analysis results in a lower lift coefficient, it may still constitute an overestimate because there may be a separation that is not captured by the Eulerian model; since the velocities are still low, the result is still considered accurate.

With regard to the transonic regime, it is expected that Raymer's model tends to underestimate the lift coefficient, especially at high incidences, for the reasons explained above. The CFD analysis, on the other hand, appears to overestimate the C_L , due to the chosen model, the Eulerian model.

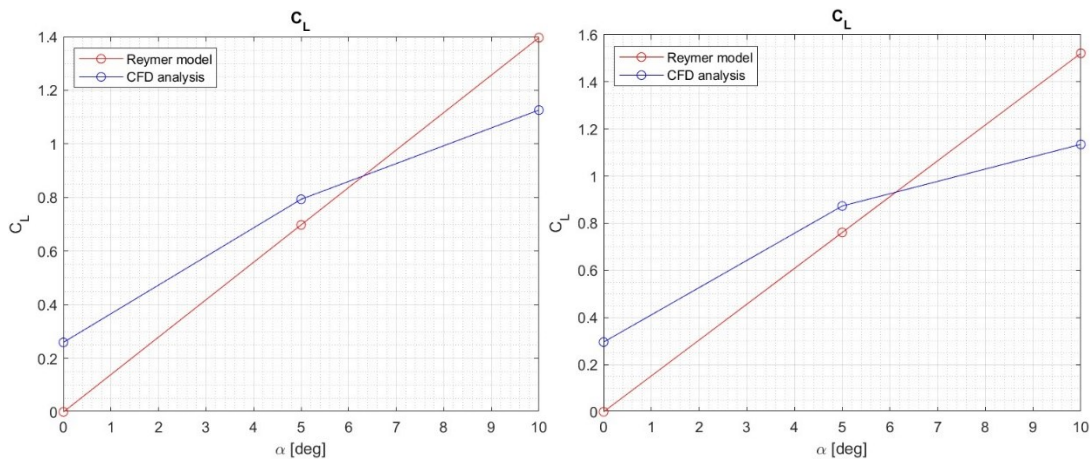


Figure 5.1: Lift coefficient - $M=0.3$, $M=0.6$

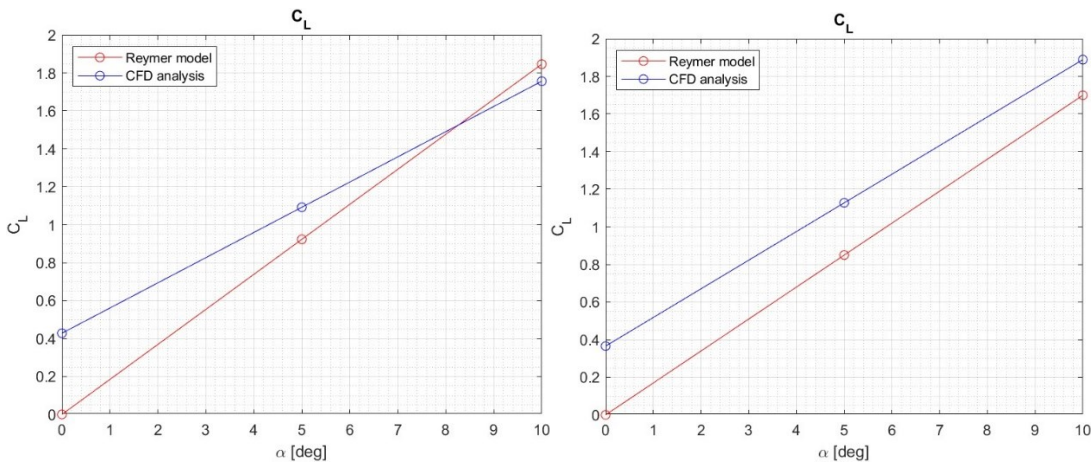


Figure 5.2: Lift coefficient - $M=0.8$, $M=0.9$

5.1.2 Comparison of Raymer model and CFD results – Drag coefficient

The drag estimate made by applying Raymer's model includes the sum of the contribution of induced drag and parasitic drag, the former estimated with good accuracy considering the aspect ratio and wing efficiency, while the latter may be underestimated as it does not include either vortical separation or local turbulence. The CFD analysis, on the other hand, being

Eulerian, considers all the contributions of drag, hence also wave drag, which, however, is negligible in subsonic, but does not calculate parasitic drag due to viscous stresses, nor the effects related to flow separation.

At Mach numbers of 0.30 and 0.60, Raymer's model tends to estimate the drag correctly as it correctly balances induced and parasitic drag, but in the transonic regime the wave drag may turn out to be underestimated as its increase is considerable at such high speeds. The CFD analysis, not considering viscosity due to the chosen model, underestimates the drag coefficient, although it correctly estimates the wave drag.

Given these considerations, it is expected that the values of the drag coefficient calculated by means of the CFD analysis will assume lower values than those obtained by applying the Raymer model. This aspect is confirmed for Mach numbers 0.30, 0.60 and 0.80, as can be seen in the Graphs in Figures 5.3 and 5.4. At Mach 0.90, on the other hand, the opposite of what was expected is obtained, i.e. the CFD analysis gives higher drag coefficients than those of the Raymer model; this is probably due to the fact that, at such speeds, wave drag is not captured in this second procedure, as is parasitic drag; in CFD, on the other hand, wave drag is modelled well and parasitic drag is also missing, so this method gives generally higher drag coefficients.

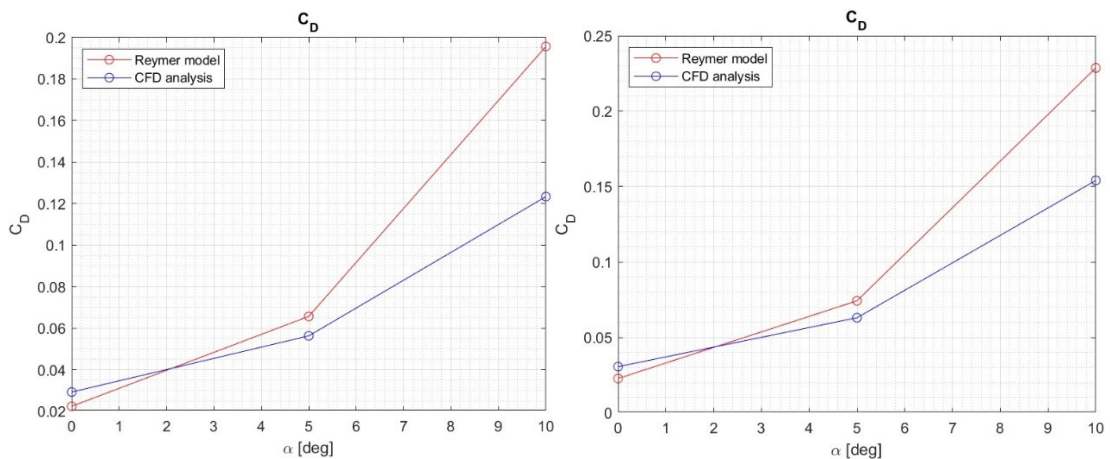


Figure 5.3: Drag coefficient - $M=0.3$, $M=0.6$

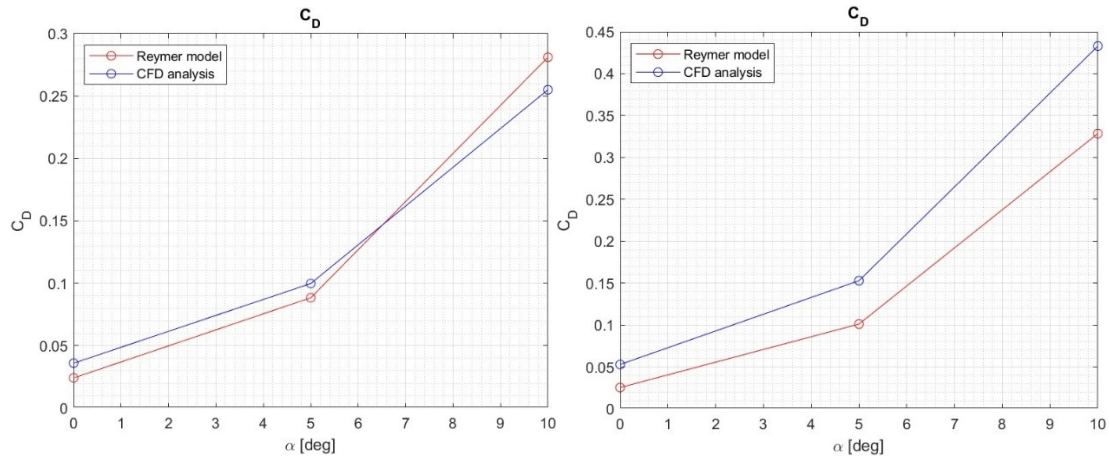


Figure 5.4: Drag coefficient - $M=0.8$, $M=0.9$

5.2 Discussion of Propulsion System simulation's results

5.2.1 Mattingly Equations Considerations

Mattingly's equations, exploited to obtain the thruster performance presented in Chapter 3, are based on certain simplifications, including the condition of ideal, stationary flow and the assumption that thruster components do not interact with each other. In real engines, these conditions do not occur as isentropic processes are often not found because both mechanical and thermodynamic losses are present, since each component has its own efficiency; vibrations and fluctuations, on the other hand, do not allow stationary flow to develop. With regard to the independence of the components, it is evident that in a real engine, complex processes take place involving the interaction of the various elements.

Having said this, it can be said that the outputs of the Mattingly equations will be affected by an error; in particular, the thrust is overestimated, especially in those cases requiring maximum thrust, where losses are important and are not taken into account in the equations. The overestimation of thrust could be around 5-15% of the actual thrust, which means that, taking the most significant thrusts presented in Table 3.7 as a reference, the actual values that should be encountered are those shown in Table 5.1.

Flight phase	T_{scal} [N]	$T_{scal,actual}$ [N]
<i>Take-off</i>	37352	31749÷35484
<i>Landing</i>	31448	26730÷29875
<i>Cruise</i>	25182	21404÷23923
<i>Maximum Mach Cruise</i>	26336	22385÷25019

Table 5.1: Estimation of actual thrust values

The SFC, on the other hand, turns out to have lower values than the real ones because the equations provide an ideal SFC because, for example, they do not take into account additional losses in the combustor, such as the efficiency of the air-fuel mixture, or even imperfect combustion and the related thermodynamic losses. The reduction of TSFC amounts to about 5-10% of the real value. Table 5.2 shows the estimated real TSFC values.

Flight phase	TSFC [kg/N s]	TSFC_{actual} [kg/N s]
<i>Take-off</i>	1.1437e-05	(1.2009÷1.2581)e-05
<i>Landing</i>	1.4598e-06	(1.5328÷1.6058)e-06
<i>Cruise</i>	1.2879e-05	(1.3523÷1.4167)e-05
<i>Maximum Mach Cruise</i>	1.9230e-05	(2.0191÷2.1153)e-05

Table 5.2: Estimation of actual SFC values

5.2.2 Nominal Thrust Considerations

The manufacturer of the engine that will be mounted on the Falcon 10 X, Rolls Royce, has declared a nominal thrust at take-off of over 81200 N for the Pearl 10 X. Since in general one can estimate a cruising thrust of 75-80% of the nominal thrust, in Table 5.3 we tried to verify the goodness of the results using this figure.

T_{nominal} [N]	T_{cruise} expected [N]	T_{cruise} calculated [N]	T_{cruise} calculated, with model-related reduction of 5-15% [N]
>81200	60900-64960	99533	69673-84603

Table 5.3: Nominal Thrust considerations

It can be seen that the calculated thrust, although reduced as mentioned in Sub-section 5.2.1, is still much higher than the nominal thrust declared by the manufacturer. This inconsistency can be traced back to the choice of inputs, since the Mattingly's equations are very sensitive to them; after a preliminary analysis, such as the one conducted in this thesis, one can think of choosing the efficiencies of the various components of the power unit not from those proposed by Mattingly, but by looking for more reliable data, relative to more modern turbofan models with higher bypass ratio. It should also be remembered that the TIT was chosen on the basis of a trend, as explained above, so it is possible that its actual value is lower than 2000 K, contrary to what was predicted.

5.3 Discussion of mission simulation's results

5.3.1 Low fidelity analysis

The aerodynamic database obtained as a result of applying the Raymer model was included in the low-fidelity analysis. The mission lasts, in total, about 15 hours; the cruise is performed at an average Mach number of 0.85 at an altitude of 12000 m. The entire operation involves the consumption of 18358 kg of fuel, so the mission is completed without using up all the available propellant.

The distance travelled operating a mission as described can be calculated by obtaining the time vector, flight path velocity and flight path angle (expressed in radians) from ASTOS. As a first step, ground velocity can be derived using the following relationship:

$$\text{ground velocity} = \text{flight path velocity} * \cos(\text{flight path angle})$$

Having obtained the ground velocity, hereafter referred to as gv , the distance flown can be calculated. Considering two successive instants of time, t_1 and t_2 , we can write:

$$\text{distance flown}(t_2) = \frac{gv(t_2) + gv(t_1)}{2} \cdot (t_2 - t_1) + \text{distance flown}(t_1)$$

The distance flown at the end of the mission is 14500 km. This value is about 11.6% greater than the one stated by the Falcon 10 X manufacturer; the comparison between range and distance flown is presented in Table 5.4.

<i>Distance flown after 15 hours [km]</i>	15500
<i>Falcon 10 X range [km]</i>	13890

Table 5.4: Comparison of distance flown and declared range – Low fidelity analysis

It can be concluded that Raymer's model fronts aerodynamic coefficients that compensate for the overestimation of the thruster's performance; although the thrust considered is much higher than the real thruster will be able to deliver, with this aerodynamic model the mission is completed exceeding the range and without consuming the entire fuel, giving an optimistic character to the low-fidelity analysis. To understand how this spills over into the calculation of the CO2 metric, see Section 5.4.

5.3.2 High fidelity analysis

The aerodynamic database obtained as a result of applying the Raymer model was included in the low-fidelity analysis. The mission lasts, in total, about 15 hours; the cruise is performed at an average Mach number of 0.75 at an altitude of 15500 m. The entire operation involves the consumption of all available fuel.

The distance travelled operating a mission as described can be calculated using the formulae presented in Sub-section 5.3.1 and the result is presented and compared with that declared by Dassault in Table 5.5. The calculated range is 1.51% higher than expected.

<i>Distance flown after 15 hours [km]</i>	14100
<i>Falcon 10 X range [km]</i>	13890

Table 5.5: Comparison of distance flown and declared range – High fidelity analysis

5.3.3 Comparison of Mission Profiles

In order to understand what is the impact of applying two different methods for the evaluation of aerodynamic coefficients, it is possible to superimpose the mission profiles obtained from the low-fidelity and the high-fidelity analysis, knowing that for each mission the requisite duration of approximately 15 hours was imposed. A first comparison can be made by displaying the altitude profiles in the same graph, presented in Figure 5.5. The difference between the two altitudes is 3.50 km and the reason for this is the higher lift that develops in the case of the high-fidelity analysis, resulting from having higher lift coefficients as a result of the CFD analysis. In the case just mentioned, in fact, even with little thrust, the aircraft tends to climb very high, reaching what is the maximum cruising altitude envisaged by Dassault.

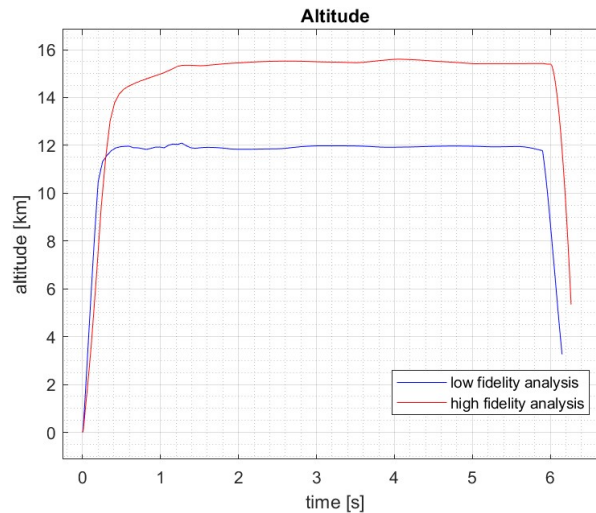


Figure 5.5: Altitude comparison - Low-fidelity vs. high-fidelity analysis

In a second step, the trend of the Mach number in the two cases can be represented, which can be seen in the graph in Figure 5.6. In the case of the high-fidelity analysis, the drag coefficient at Mach numbers of 0.80 and 0.90 and the angles of attack typical of the cruise phase (between 0° and 5°) are such that they generate higher fuel consumption in the unit of time than in the case of the low-fidelity analysis. This fact, together with the limitation imposed

by the maximum cruise altitude and the mission duration requirement, meant that the thrust used to carry out the cruise in the high fidelity case was such as to generate speeds involving Mach numbers between 0.75 and 0.82, below the value prescribed by Dassault, which is 0.85.

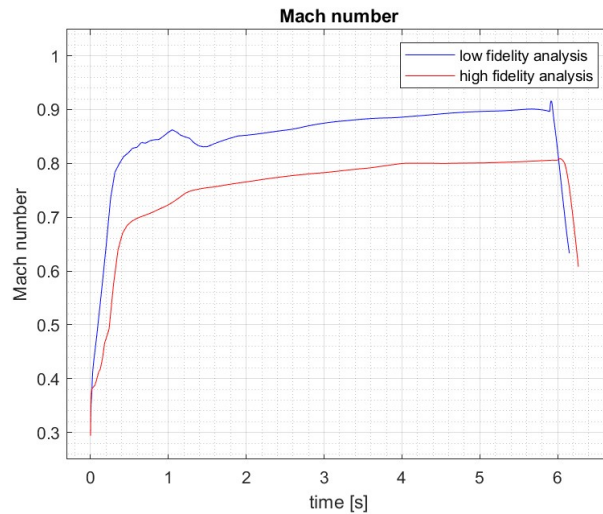


Figure 5.6: Mach number comparison - Low-fidelity vs. high-fidelity analysis

5.4 Discussion of CO₂ metric values obtained

5.4.1 The low fidelity CO₂ metric value: based on present masspoints vs based on real cruise points

In Chapter 3, a CO₂ metric value of 0.4574 was obtained through the application of the standard. The arrangement of the gross masses on the mission profile is sufficiently symmetrical and, in particular, the mid gross mass is located exactly at mid-cruise; in general, when regulations are applied to an aircraft, the gross masses are arranged approximately at the beginning (high gross mass), middle (mid gross mass) and end of cruise (low gross mass). Observing, then, the arrangement of the gross masses on the mission profile prepared for the case study (Figure 3.14), it can be seen that the low gross mass and the high gross mass deviate from the points just mentioned.

In order to understand how the metric value of CO₂ would change if the position of the gross masses on the mission profile were to be respected, a repositioning of the same is carried out, exploiting the Mach number profile in Figure 5.7; this is necessary because the start of the cruise phase is identified with the attainment of the cruise Mach, equal to 0.80.

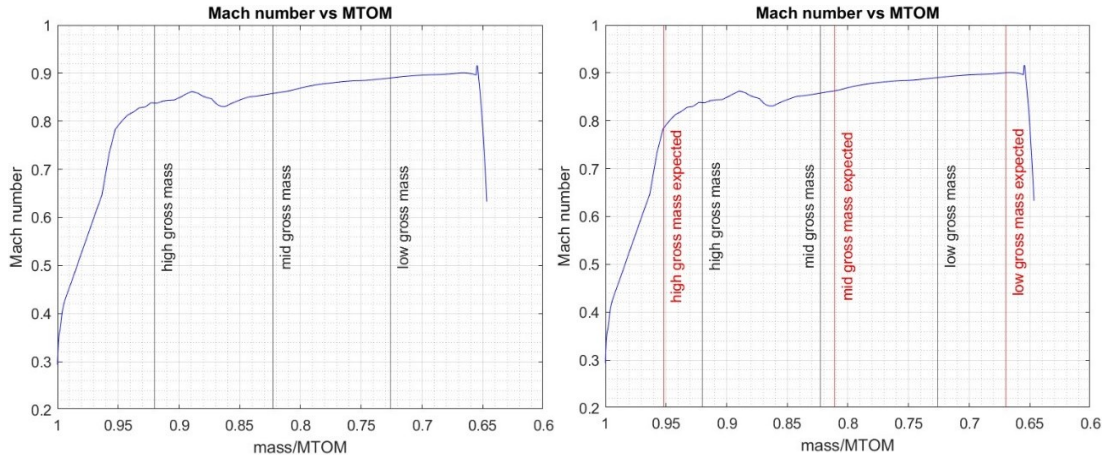


Figure 5.7: Gross masses within the Mach number profile – Low fidelity analysis

Thus, the new expressions for calculating gross masses are:

$$\text{high gross mass} = 0.952 \cdot \text{MTOM}$$

$$\text{low gross mass} = 0.667 \cdot \text{MTOM}$$

The mid gross mass is again calculated as the average of the other two masses; the values obtained are shown in Table 5.5.

	Old	New
High gross mass [kg]	47990	49659
Low gross mass [kg]	37867	34935
Mid gross mass [kg]	42929	42297

Table 5.6: New gross masses vs old ones

Once the new masses have been found, the SAR can be recalculated, the values of which are given in Table 5.4. To understand how these masses also fit into the SAR profile, look at Figure 5.6.

	SAR [km/kg]	1/SAR [km/kg]	$\left(\frac{1}{\text{SAR}}\right)_{\text{AVG}}$ [km/kg]
<i>High gross mass</i>	502.99	1.9881e-3	1.2867e-3
<i>Low gross mass</i>	1112.7	9.7341e-4	
<i>Mid gross mass</i>	1027.3	8.9864e-3	

Table 5.7: $\left(\frac{1}{\text{SAR}}\right)_{\text{AVG}}$ calculation

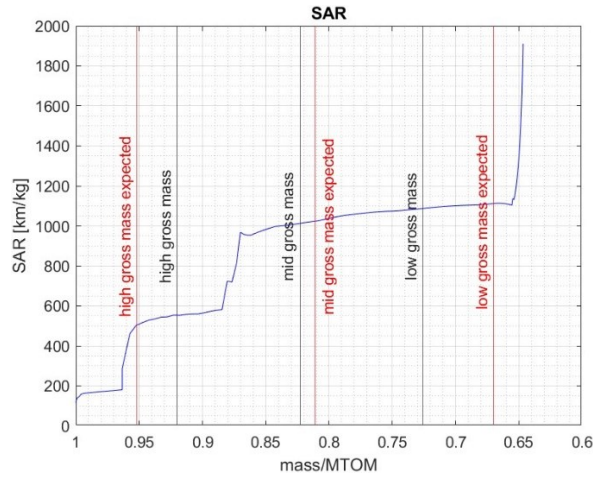


Figure 5.8: New gross masses within the Mach number profile – Low fidelity analysis

The RGF was previously calculated, so it is possible to obtain the new metric value of CO₂, based on real cruise points, shown in Table 5.8.

<i>CO₂ metric value (based on present mass points) [kg/km]</i>	0.4574
<i>CO₂ metric value (based on real cruise points) [kg/km]</i>	0.4761

Table 5.8: Comparison of the two CO₂ metric values

Taking the one calculated on the basis of real cruise points as the exact value, the percentage deviation between the two can be calculated, multiplying the following expression by 100:

$$\frac{|CO_2 \text{ metric value}_{\text{based on real cruise points}} - CO_2 \text{ metric value}_{\text{based on present masspoints}}|}{CO_2 \text{ metric value}_{\text{based on real cruise points}}}$$

An error of 3.92% is obtained, so it can be concluded that the results of the low-fidelity analysis are acceptable, despite the fact that the placement of the gross masses on the mission profile is not exactly as expected.

Another comparison can be made with the max permitted CO₂ metric value: both the value calculated on the basis of present masspoints and that calculated on the basis of real cruise points are well within the limit imposed by the regulations. In particular, considering that a maximum permitted value of 0.7208 was obtained for the case study, and taking into account the metric values calculated for the low-fidelity analysis, we have that:

- The CO₂ metric value based on the present masspoints is 35% lower than the maximum permitted value;
- The CO₂ metric value based on the real cruise points is 32% lower than the maximum permitted value.

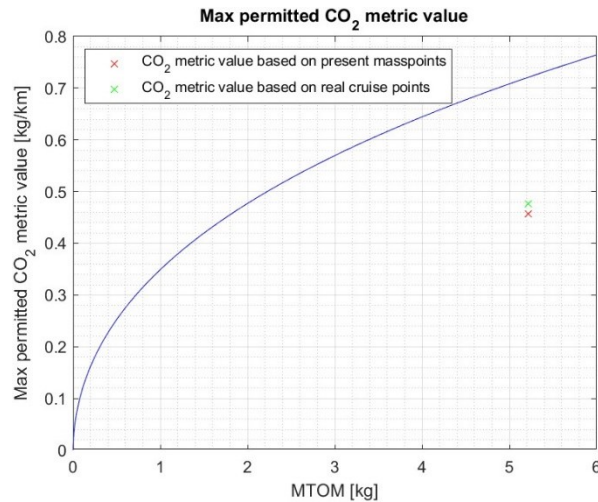


Figure 5.9: Comparison of the two CO₂ metric values and max permitted CO₂ value – Low fidelity analysis

5.4.2 The high fidelity CO₂ metric value: based on present masspoints vs based on real cruise points

In Chapter 4, a CO₂ metric value of 0.7494 was obtained through the application of the standard. Values of C_L higher in the case of high fidelity analysis means that higher rates are reached at lower speeds, at the same time the values of C_D higher at Mach numbers close to cruise speed result in higher fuel consumption. This results, in the first case in a lower TAS, which will therefore lead to a lower SAR, and in the second case in a higher fuel flow, which contributes to a lower SAR. Poichè nel calcolo del valore metrico di CO₂ va inserito l'inverso del SAR, tutto questo si traduce in un valore metrico più elevato rispetto al caso low. Since the inverse of SAR must be included in the calculation of the CO₂ metric value, this results in a higher metric value than in the low case. On the other hand, the higher fuel consumption for the same phase duration results in a shift of gross masses towards the initial cruise phase because the aircraft 'lightens up' faster, in terms of time. Having masses so arranged and lower velocities at those points results in a higher CO₂ metric value than the low-fidelity case, and is also expected to be higher than the same value calculated by repositioning the masses at the beginning (high gross mass), middle (mid gross mass) and end of cruise (low gross mass).

In order to understand how the metric value of CO₂ would change if the position of the gross masses on the mission profile were to be respected, a repositioning of the same is carried out, exploiting the Mach number profile in Figure 5.10; this is necessary because the start of the cruise phase is identified with the attainment of the cruise Mach, equal to 0.70.

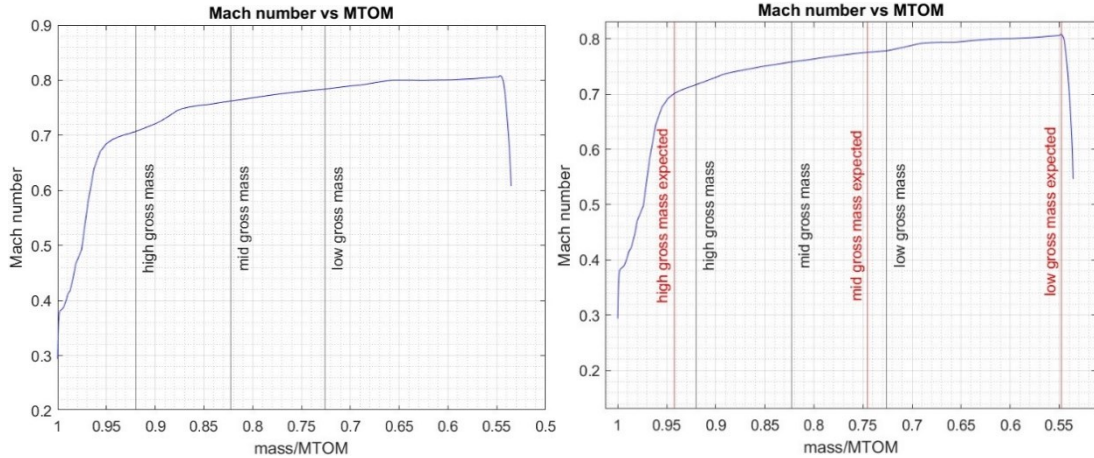


Figure 5.10: Gross masses within the Mach number profile – High fidelity analysis

Thus, the new expressions for calculating gross masses are:

$$\text{high gross mass} = 0.932 \cdot \text{MTOM}$$

$$\text{low gross mass} = 0.548 \cdot \text{MTOM}$$

The mid gross mass is again calculated as the average of the other two masses; the values obtained are shown in Table 5.9.

	Old	New
High gross mass [kg]	47990	48626
Low gross mass [kg]	37867	28512
Mid gross mass [kg]	42929	38569

Table 5.9: New gross masses vs old ones

Once the new masses have been found, the SAR can be recalculated, the values of which are given in Table 5.10. To understand how these masses also fit into the SAR profile, look at Figure 5.11.

	SAR [km/kg]	1/SAR [km/kg]	$\left(\frac{1}{\text{SAR}}\right)_{\text{AVG}}$ [km/kg]
High gross mass	387.10	2.5833e-3	1.7911e-3
Low gross mass	905.63	1.1042e-4	
Mid gross mass	593.16	1.6859e-4	

Table 5.10: $\left(\frac{1}{\text{SAR}}\right)_{\text{AVG}}$ calculation

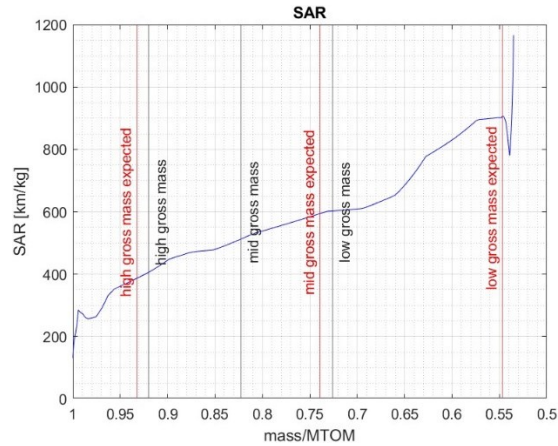


Figure 5.11: New gross masses within the Mach number profile – Low fidelity analysis

The RGF was previously calculated, so it is possible to obtain the new metric value of CO₂, based on real cruise points, shown in Table 5.11.

<i>CO₂ metric value (based on present mass points) [kg/km]</i>	0.7494
<i>CO₂ metric value (based on real cruise points) [kg/km]</i>	0.6627

Table 5.11: Comparison of the two CO₂ metric values

Taking the one calculated on the basis of real cruise points as the exact value, the percentage deviation between the two is 13.43%.

Another comparison can be made with the max permitted CO₂ metric value: the value calculated on the basis of present masspoints exceeds the maximum permitted value, while that calculated on the basis of real cruise points is within the limit imposed by the standard. In particular, considering that a maximum permitted value of 0.7208 was obtained and taking into account the metric values calculated for the low-fidelity analysis, we have that:

- The CO₂ metric value based on the present masspoints is 4.0% higher than the maximum permitted value;
- The CO₂ metric value based on the real cruise points is 8.1% lower than the maximum permitted value.

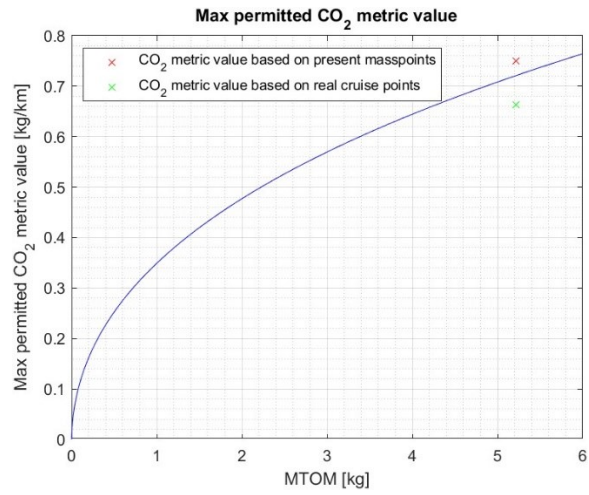


Figure 5.12: Comparison of the two CO₂ metric values and max permitted CO₂ value – High fidelity analysis

Capitolo 6

CONCLUSIONS

The case of the low-fidelity analysis, although it allows the mission to be realised by satisfying all the requirements, including mission duration, range, altitude and cruising Mach number, does not turn out to be sufficiently close to reality, since the aerodynamic coefficients are decidedly underestimated by Raymer's model. In this case, in fact, higher speeds are reached because in order to climb in altitude with reduced lift coefficients, it is necessary to intervene by increasing the throttle, which, however, due to the reduced drag at cruising Mach, must remain contained in order to meet the Mach number requirement: hence the mission ends by exceeding the range envisaged by Dassault by 12%, but consuming only 80% of the fuel. It is evident, then, that the CO₂ metric value resulting from the low-fidelity analysis is also affected by error and, in particular, is over-optimistic.

The case of the high fidelity analysis, despite the fact that both range and altitude requirements are met, does not see a mission carried out at the Mach number of 0.85 declared by Dassault, but is carried out at an average Mach number of 0.75. Despite this, this can be considered the case closest to reality, since it starts from more reliable data, as far as aerodynamics are concerned, thanks to the use of CFD. The result obtained can also be considered more realistic by reasoning a posteriori, i.e. by observing that the fuel is used in its entirety to complete a mission on schedule and covering exactly the distance declared by the manufacturer, at the maximum possible altitude.

The application of the standard to the aeroplane considered as a case study, given the hypotheses and simplifications made, does not give a positive outcome, since the metric value of CO₂ exceeds the maximum allowed: the study made determines, therefore, the non-conformity of the aeroplane to the standard, therefore it could not be certified. It should be noted, however, that the relationships that allow for the calculation of high gross mass and low gross mass in the standard are designed to generate mass values that are placed in the mission profile at the beginning and end of the cruise phase respectively; this is done to take into account the fact that most of the fuel is consumed during this phase and that, therefore, it is here that most of the CO₂ is generated. In the case of the mission obtained, this placement is

not respected for the reasons expressed in Sub-section 5.4.2, suggesting an inadequacy of the regulations to properly fit the aircraft's emissions.

The aim was then to see how the metric value of CO₂ might change if more realistic mass values were obtained instead. By making the necessary corrections, i.e. repositioning the gross masses where they would be more effective in describing the CO₂ emissions of the aircraft, it was seen that the metric value obtained is within the limit imposed by the standard. On the basis of this result, what was expected is confirmed, namely that in order to better frame the business jet category, changes should be made at least to the relationships that place the masses within the mission profile, since it is from them that the entire calculation chain leading to the evaluation of the CO₂ metric value starts; if, in fact, there were other aircraft belonging to this category that showed similar behaviour, the application of the regulations would be critical.

In order to make a modification to the calculation of high gross mass and low gross mass, it would be necessary to perform the same analysis on a statistically significant number of aircraft, belonging to the business jet category. If a preliminary CO₂ analysis were carried out for each of them following the logic of this thesis, this would lead to a definition of the new masses, again expressed as a percentage of MTOM, that could adequately cover the performance of the entire category. One would thus obtain:

$$\text{high gross mass} = c_1 \cdot \text{MTOM}$$

$$\text{low gross mass} = c_2 \cdot \text{MTOM}$$

$$\text{mid gross mass} = \text{average}(\text{high gross mass}, \text{low gross mass})$$

Where c_1 and c_2 are the result of the statistics performed. As far as the maximum CO₂ metric value is concerned, having studied only one aircraft, it is not possible to make considerations on it.

If the result obtained is confirmed by the study of other similar aircraft, on the basis of purely mathematical calculations and considerations, it can be stated that a revision of the regulations should be carried out to better include the business jet category or, alternatively, a dedicated section should be added. With regard to the maximum limit to be imposed on CO₂ emissions, the mathematical tool alone does not allow for any reflections on this, since it is the result of compromises between states adhering to ICAO standards and aircraft and engine manufacturers; it is very likely that regulations in the future will attempt to adapt in this respect as well, especially if, referring to the data set out in Section 1.5, consideration is given to the type of use made of business jets and especially the frequency with which they are used.

REFERENCES

Lucy Budd and Phil Hubbard, *The 'Bizjet set': Business aviation and the social geographies of private flight*, International business travel in the global economy, Loughborough University, England, 2016.

Junzi Sun, Xavier Olive and Martin Strohmeier, *Environmental Footprint of Private and Business Jets, Engineering proceeds*, MDPI, Delft University of Technology, 2628 CE Delft, The Netherlands.

National Business Aviation Association (NBAA), *Business Aircraft Uses* (www.nbaa.org).

Iba, *Changing Tides: Business Jets Experience a Dip in Demand*, 9 Febbraio 2024 (www.iba.aero).

Chapman Freeborn, *Private jet classifications and capabilities*, 5 Giugno 2023 (www.chapmanfreeborn.aero).

Todd Spangler, *Private Jet Categories*, JetStream, 29 Novembre 2021 (www.jetcraft.com).

The Basics of Private Jet Categories, JetStream, 30 Giugno 2015 (www.jetcraft.com).

Raymond Jaworowski and Douglas Royce, *The Market for Business Jet Aircraft 2023-2032*, Forecast International.

The postal history of ICAO, Annex 16 – Environmental Protection, ICAO (www.icao.int).

Kerry Lynch, *Dassault Building Components, Testing Systems on Falcon 10X*, AIN, 27 Maggio 2024 (www.ainonline.com).

Falcon 10 X, Dassault Aviation (www.dassaultaviation.com).

Falcon 10X, The large business jet segment redefined, Dassault Falcon (www.dassaultfalcon.com).

Pearl 10 X, Rolls-Royce (www.rollsroyce.com).

Fabio Amoretti, Edoardo Briano, Marco Cancaro, Giorgia Castorina, Paolo Cesano, Marco Crudo, Alfredo Esposito, Federico Filippini, Antonio Giacobbe, Fabio Longo Vaschetti, Alessandro Pasqualini, Marco Tituccio, Alberto Tomatis, Alessandro Vitega, *Design of a Ultra-Long Business Jet*, Progetto del Corso di “Progetto dei sistemi aerospaziali integrati”, Politecnico di Torino, Torino, 2024.

Daniel P. Raymer, *Aircraft Design: A Conceptual Approach*, American Institute of Aeronautics and Astronautics, 2018.

Oscar Gori, *Methodology and Tools for High-Speed Vehicles Conceptual Design to Support Environmental Regulations*, Politecnico di Torino, Italy, 2024.

Jack D. Mattingly, *Elements of Gas Turbine propulsion*, McGraw-Hill Education, New York, New York, Stati Uniti, 1995.

Ahmed F. El-sayed, Mohamed S. Emeara, Mohamed A. El-habet, *Performance Analysis of High Bypass Ratio Turbofan Aeroengine*, International Journal of Development Research 6(07):8382-8398, July 2016.

International Civil Aviation Organization, *CO₂ Certification Requirement*, Annex 16 – Volume III, 03/06/2017.

Ansys Fluent - Fluid Simulation Software, Ansys (www.ansys.com).

Samuele Graziani, Francesco Petrosino, Jacob Jäschke, Antimo Glorioso, Roberta Fusaro, Nicole Viola, *Evaluation of Sonic Boom Shock Wave Generation with CFD Methods*, Aerospace 2024.

P. L. Roe, *Characteristic-Based schemes for the Euler equations*, College of Aeronautics, Cranfield Institute of Technology, Cranfield MK43 0AL, England, 1986.

Domenic D'Ambrosio, *Hyperbolic Equations*, Dispense del Corso di “Fluidodinamica computazionale”, Politecnico di Torino, Torino, 2022.

Rosell, D., Grönstedt, T., *Design Considerations of Low Bypass Ratio Mixed Flow Turbofan Engines with Large Power Extraction*. Fluids, 2022.